ADVANCED FUNCTIONAL MATERIALS
www.afm-journal.de

Coherent Single-Atom Dipole–Dipole Coupling Mediates Holistic Regulation of K^+ Migration for Superior Energy Storage and Dendrite-Free Metal Deposition

*Yen-Yang Tseng and Hsing-Yu Tuan**

Potassium-based batteries, including potassium-ion (PIBs) and potassium metal batteries (PMBs), are gaining attention as alternatives to lithium-ion batteries (LIBs). However, potassium's large ionic radius (1.38 Å) reduces charge density, weakens solvation, and increases energy barriers for K^+ diffusion, leading to slower reaction kinetics, thicker solid electrolyte interphase (SEI) layers, and dendrite formation. To address these challenges, a novel single-atom Fe-N_4 dipole–dipole coupling (SA.Fe) is proposed. The unique Fe-N_4 coordination and highly conductive Ketjen black (KB) substrate establish a rapid horizontal electron transfer network, enhancing electrode interface reactions. Moreover, Fe-N-C coordination generates a short-range polar electric field, improving K^+ affinity and diffusion. This coherent single-atom coupling effectively regulates K^+ migration, significantly enhancing reaction kinetics and lowering diffusion barriers. The SA.Fe anode delivers high reversible capacities (446.3 mAh g^{-1}) and exceptional durability (10 000 cycles at 2.0 A g^{-1}) in PIBs, alongside remarkable stability (600 cycles at 0.5 mA cm^{-2}) and fast potassium metal (K metal) deposition without dendrite formation in PMBs. This study highlights the potential of coherent single-atom dipole coupling for efficient K^+ storage and dendrite-free batteries, offering a promising pathway for next-generation potassium-based energy systems.

1. Introduction

Potassium-based batteries are a promising alternative to lithium-ion batteries (LIBs). Regarding the potassium-ion batteries (PIBs),[1–15] the potassium's abundance and chemical similarity to lithium give rise to the superior ion storage performance. Meanwhile, potassium metal batteries (PMBs)[16–21] have garnered attention for their significantly higher energy density and lower potential of potassium metal (−2.93 V vs standard hydrogen electrode). However, potassium's inherent properties limit K^+ reaction kinetics, resulting in poor energy storage performance. The larger ionic radius of potassium (1.38 Å) reduces charge density and weakens the solvation effect. The low charge density of K^+ leads to an unstable solvation shell that breaks down at the electrolyte-electrode interface,[22–24] limiting reaction kinetics, thus reducing storage capacity. Carbonaceous materials can develop positively charged defects, worsening K^+ adsorption and further decreasing capacity. In PMB systems, these positively charged regions impede uniform K^+ diffusion, leading to localized concentration and increased dendrite formation risk. Additionally, the larger ionic radius and unstable solvation shell result in a thicker, unstable SEI layer that raises interface resistance and restricts K^+ migration, promoting Volmer–Weber (V–W) type metal deposition and dendrite formation. Consequently, effective holistic regulation of K^+ migration is essential for achieving superior electrochemical performance in both PIBs and PMBs.

The electric potential difference and electric field at material interfaces are crucial parameters in potassium-based batteries. Electric field modulation is considered one of the most effective methods for achieving high-performance K^+ storage. A classic example is the concept of interface electric fields (IEF).[25–28] The concept utilizes the built-in electric fields induced at heterogeneous interfaces between different phases to attract charges and ions, accelerating the movement in specific reaction directions. Orbital hybridization at these interfaces provides more electrons available for reaction, which effectively promotes charge transfer and ion diffusion. The concept can be also applied in the PMBs.[29–32] The dendrite formation can be suppressed by reducing local current density and promoting uniform deposition. The benefit of electric field modification can be demonstrated by Song et al.'s research.[33] The interface electric field is optimized by $FeSe/Fe_3Se_4$ heterostructure, which significantly improved reaction kinetics and structural stability. Additionally,, ultrafine high-entropy nano-modified particles were used to create a buffering layer on zinc metal anodes, highlighting the guiding role of electric field modulation in metal deposition.[34] However, lattice materials, commonly used for electric field modulation, face challenges in stress adjustment due to volumetric expansion during charge-discharge

Y.-Y. Tseng, H.-Y. Tuan
Department of Chemical Engineering
National Tsing Hua University
Hsinchu 30013, Taiwan
E-mail: hytuan@che.nthu.edu.tw

The ORCID identification number(s) for the author(s) of this article can be found under https://doi.org/10.1002/adfm.202423387

DOI: 10.1002/adfm.202423387

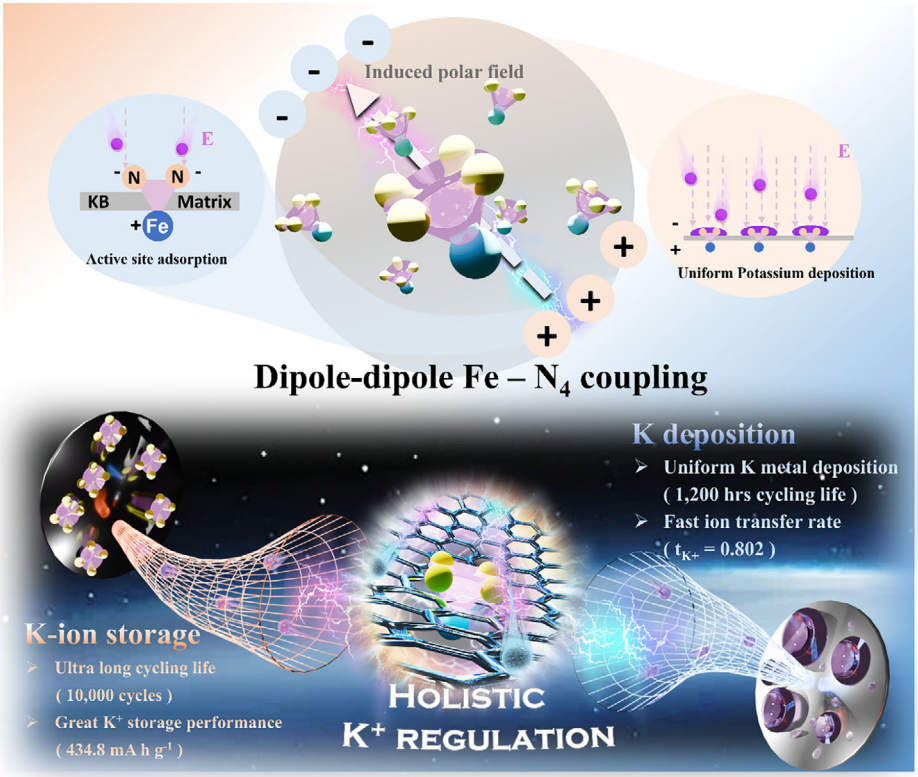

Figure 1. The schematic illustration of the feature of SA.Fe and the corresponding built-in polar electric field.

cycles, leading to reduced cycle life compared to carbon-based materials, thus limiting their practical applications.

Single-atom materials (SAMs) maximize atomic efficiency by isolating metal atoms on conductive substrates,[35–40] unlocking their full catalytic potential.[41] By coordinating single transition metal (TM) atoms with nearby atoms, the interaction between TM d orbitals and adjacent p orbitals redistributes electrons. This effective electron regulation enhances catalytic activity and suppresses side reactions, which is commonly observed in catalytic reactions such as hydrogen evolution.[42–45] Recently, SAMs have been adopted as effective anodes in potassium-based batteries. Studies have demonstrated that modulation of electronic structures significantly benefits the electrochemical performance. Specifically, SAMs enhance overall reaction kinetics, including charge transfer, reactant affinity, and K^+ adsorption. This modulation adjusts adsorption energy and lowers energy barriers, leading to improved cycling performance and K^+ storage efficiency, while delivering a high specific capacity. For instance, Zn single atoms on carbon substrates improve K^+ storage, achieving a specific capacity of 350 mAh g^{-1} at 0.1 A g^{-1}, along with 90.2% capacity retention after 4000 cycles at 2 A g^{-1}.[46] Xu et al. proposed a manganese ion-catalyzed mechanism to regulate electron distribution in hard carbon, significantly enhancing K^+ plateau storage and initial Coulombic efficiency (ICE). This modulated hard carbon exhibits a high low-potential plateau capacity of 272.6 mAh g^{-1}.[47] Furthermore, the reduced potential around the central TM atom generates a localized microelectric field on the catalyst surface. Wang et al. reported that introducing Fe-N_4 structures induces charge rearrangement and an uneven charge distribution.[48–50] Electrostatic potential (ESP) simulations reveal that Fe atoms in Fe (MIL)-SAC form positively charged centers. This charge asymmetry enhances the affinity of adjacent N atoms forK^+. The generated polar field further provides the additional potential benefits, which may accelerate reaction kinetics in potassium-based batteries.

This study introduces an innovative single-atom Fe-N_4 dipole–dipole coupling (SA.Fe) design, achieved through precise π–π hybridization control (**Figure 1**). This design ensures high metal loading and extensive surface coverage, optimizing Fe-N_4 active sites to enhance K^+ kinetics. The inherent electronegativity difference between Fe and N atoms generates a localized polar electric field that boosts K^+ mobility and optimizes potassium metal deposition. The Fe-N_4 couplings are strategically anchored on a highly conductive Ketjen Black (KB) substrate, with the polar electric field forming spontaneously. These unique active units significantly enhance K^+ reaction kinetics in PIBs through the strong dipole–dipole coordination of Fe-N_4 and the adjacent S dopant. This distinctive coordination environment boosts K^+ kinetics and strengthens adsorption. In PMBs, the polar electric field establishes vertical ion transport channels, effectively guiding K^+ for uniform deposition on the material's surface, significantly reducing the risk of dendrite formation.

Overall, SA.Fe achieves remarkable improvements in K^+ storage capacity and uniform potassium metal deposition, offering

holistic regulation of K^+ migration. These advancements translate into exceptional energy storage performance and cycle stability, demonstrating SA.Fe's potential as a superior anode material for potassium-based batteries. This work demonstrates the feasibility of integrating enhanced electron transfer, ion regulation, and stable cycling for next-generation energy storage technologies.

2. Results and Discussion

2.1. Synthesis and Structural Characterization of SA.Fe

As shown in **Figure** 2a, SA.Fe with single-atom Fe-N_4 coupling was synthesized via a gradient heating pyrolysis method. π-π stacking interactions promoted a uniform Fe-N_4 distribution. Iron phthalocyanine (FePc), dicyandiamide (DCDA), and diphenyl disulfide served as Fe, N, and S sources, respectively, and were mixed with KB before calcination. At 450 °C, FePc undergoes sublimation and dehydrogenation, releasing most hydrogen atoms and forming unstable planar fragments. The fragments form the basis for single-atom coupling, with π–π interactions promoting the aggregation of similarly oriented fragments into self-assembled structures with offset parallel displacements. These interactions also enable coupling between FePc fragments and the KB substrate, creating a stable hybrid structure. As the temperature reaches 800 °C, DCDA and diphenyl disulfide decompose sequentially. DCDA releases volatile CN_x species, and diphenyl disulfide produces diphenyl sulfide and hydrogen sulfide, supplying nitrogen and sulfur for bonding with FePc to form electron-deficient Fe-N_xS fragments. This doping weakens the π–π interactions among Fe-N_xS fragments at high temperatures, causing their detachment from the self-assembled structures. This phenomenon is quantified using the vacancy concentration formula. High temperatures promote vacancy formation; at 800 °C, KB generates electron-rich vacancies and defects that disrupt its π-conjugated network. Defects, along with electron-deficient Fe-N_xS fragments, enhance coordination between KB and FePc via π–π stacking, resulting in Fe-N_xS/KB hybridization. Strong coupling prevents Fe-N_xS re-aggregation, exposing more active Fe sites and boosting catalytic activity. Significant electronegativity differences in the Fe-N_4 unit establish a polar coupling, with Fe as the electron-deficient center and N as the electron-rich counterpart, creating a distinct polar electric field in SA.Fe that enhances charge storage and electron transport efficiency.

Strong π-π interactions ensure effective dispersion, forming a uniform single-atom structure. In a control experiment, varying FePc and diphenyl disulfide ratios under consistent conditions produced high-loading Fe atomic clusters (cluster Fe), S and N-doped carbon materials (SA.sub), and N-doped carbon materials (pure sub). Figure 2b shows a HAADF-STEM image of SA.Fe, with bright spots indicating Fe atoms. HAADF relies on high-angle scattered electrons, where the scattering intensity is proportional to the square of the atomic number Z^2. To better visualize the positions of Fe-N_4 coupling, we enhanced the contrast by suppressing signals from neighboring N and S atoms while amplifying the Fe signal. Hence, the location of Fe-N_4 coupling is represented by the single-atom Fe signal. The dense, uniform, and isolated bright spots confirm the even distribution of Fe-N_4 coupling on the KB surface, aided by π–π stacking, maximizing active site exposure. In contrast, the HAADF-STEM image of cluster Fe (Figure S1, Supporting Information) shows significant Fe atom aggregation and stacking. The observation suggests that excessive FePc concentration strengthens π–π stacking within the self-assembled structures, preventing effective bonding and detachment of FePc fragments with S and N species. As a result, large FePc aggregates form on the KB surface, leading to unstable structures. The SEM image of SA.Fe (Figure 2c) shows randomly connected elliptical carbon particles, 100–200 nm in diameter, typical of the KB structure. The absence of visible Fe and S particles suggests that Fe, S, and N are dispersed at the nanometer scale within the carbon spheres. The lack of self-assembled FePc particles confirms their detachment at high temperatures. The high-magnification SEM image of SA.Fe (Figure 2d) shows a roughened carbon sphere surface, indicating successful Fe-N_xS/KB hybridization. SEM images of SA.sub, pure sub, and cluster Fe are shown in Figure S2 (Supporting Information). SA.sub retains an intact doping structure, preserving KB's original surface morphology. In contrast, pure sub and cluster Fe show smooth surfaces due to Ostwald ripening, where CN_x and Fe-N_xS fragments coalesce into larger particles to minimize surface energy. The smooth surfaces indicate a lack of doping sites, causing excess fragments to accumulate on KB, hindering K^+ adsorption.

TEM images (Figure 2e) show the elliptical spheroidal morphology of SA.Fe, confirming a solid carbon structure with no central holes or particles, indicating the absence of metal or self-assembled particles in KB. High magnification TEM (Figure 2f) reveals disordered interlayer spacing, confirming π-conjugated structure disruption due to Fe-N_xS/KB hybridization. The TEM image of cluster Fe shows a similar result to the SA.Fe (Figures S3 and S4, Supporting Information). However, A slightly wider dark region in the low magnification image indicates a more serious aggregation in cluster Fe. This increased disorder enhances the material's toughness and structural integrity. EDS mapping (Figure 2g) shows uniform distribution of S, N, and Fe species. Elemental analysis (Figure S5, Supporting Information) gives atomic ratios of C, N, S, and Fe as 92.2, 7.2, 0.5, and 0.1 At%, respectively, indicating KB as the primary component with nitrogen as the main dopant. In comparison, a higher content of Fe is observed in cluster Fe (Figure S6, Supporting Information), which gives a rise to the probability of the Fe atom aggregation. This confirms the effective combination of surface vacancies and N dopants. The iron content in SA.Fe is 0.90 wt.%, closely matching the 1.296 wt.% from ICP-MS (Table S1, Supporting Information), validating the elemental distribution accuracy. The 3D topography map (Figure 2i) confirms the single-atom nature of Fe, showing numerous high peaks corresponding to Fe atoms at the center of Fe-N_4 coupling. The well-spaced, non-stacked peaks align with HAADF-STEM results. Lower peaks represent S and N species, indicating doping near Fe atoms, confirming Fe-N_4 coupling. The intensity profiles of the selected areas in HAADF-STEM images (Figure 2h) show several distinct peaks, corresponding to the single-atom Fe, while the lower peaks labeled in orange circles represent the N and S species. The profile verifies the coordination of Fe-N_4 coupling. A spacing of ≈2.5 Å between Fe atoms

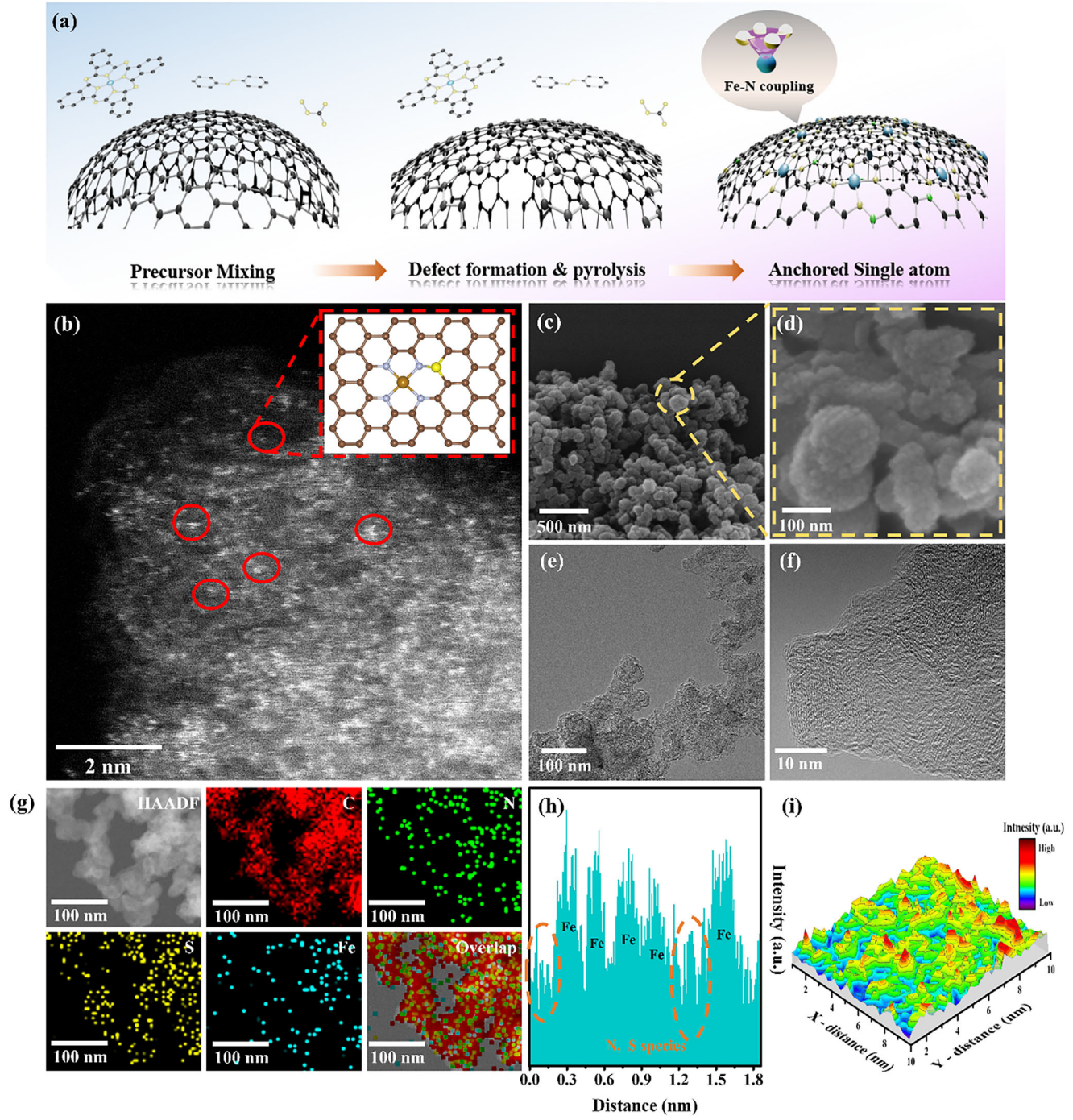

Figure 2. Synthesis and structural characterization of SA.Fe. a) Schematic illustration of the synthesis process of SA.Fe b) HAADF-STEM image, c) Low magnification SEM image, d) High magnification of SEM image, e) Low magnification TEM image, and f) High magnification TEM image of SA.Fe. g) STEM EDS mapping images of SA.Fe. h) The intensity profiles of the selected areas in SA.Fe. i) 3D topography image of SA.Fe.

is observed, indicating a densely packed Fe-N_4 coupling. SA.Fe exhibits a high-coverage, uniformly distributed Fe-N_xS/KB surface, as shown by the dense bright spots in HAADF-STEM. ICP-MS reports Fe at 1.27 wt.%, Fe-Ni at 0.45 wt.%, and Zn at 0.068 wt.%.[51–55] The iron content of 1.296 wt.% exceeds other metal loadings, confirming the high coverage and density of Fe-N_4 coupling.

2.2. Composition Characterizations of SA.Fe

Figure 3a shows the XRD spectra of SA.Fe, SA.sub, pure sub, and cluster Fe, featuring broad Bragg peaks at 26° and 43°, corresponding to the (002) and (100) planes of KB carbon structures, confirming the carbon skeleton. The degree of disorder in KB materials is assessed by the I_D/I_G ratio in Raman spectra (Figure 2b).

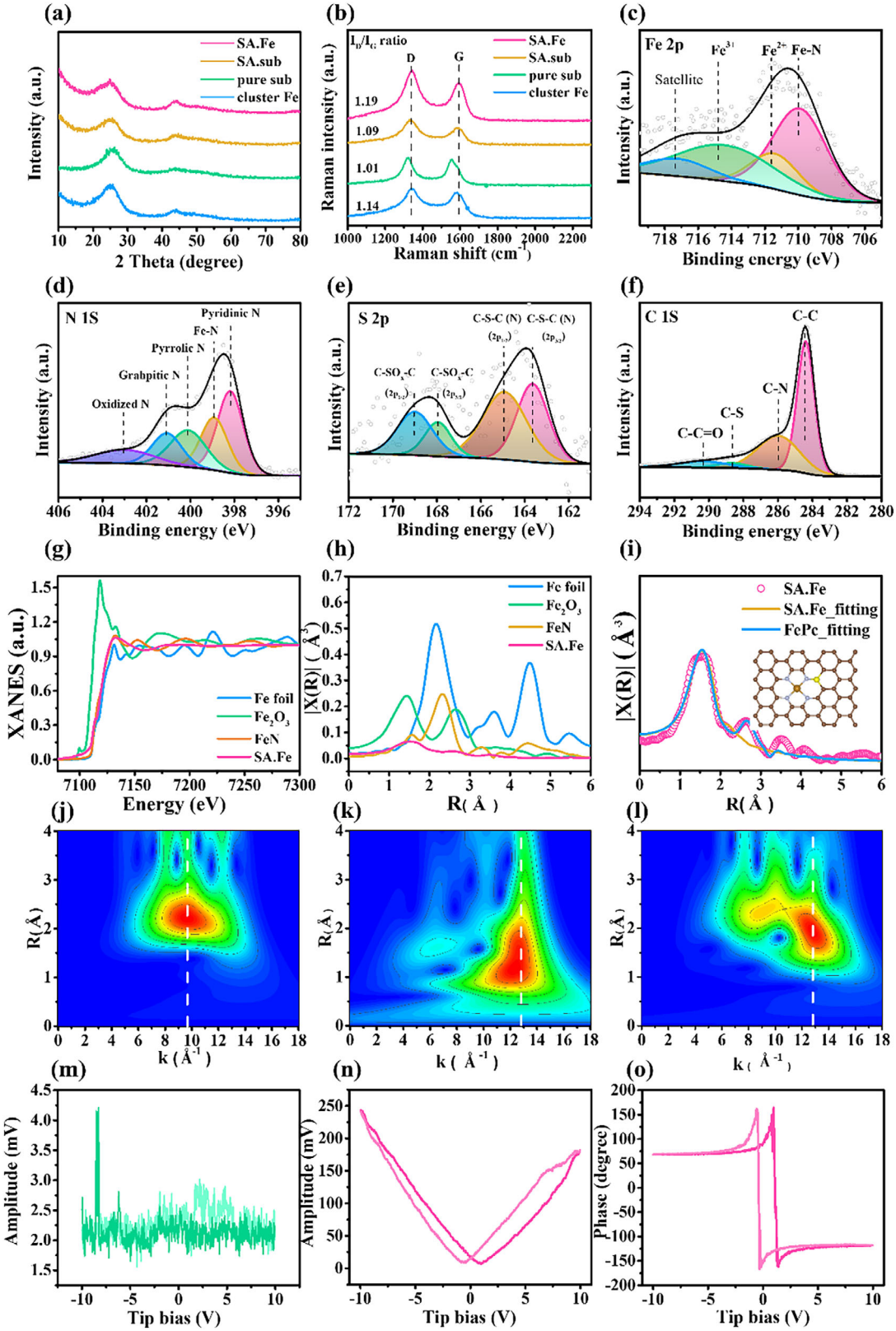

Figure 3. Composition characterizations of SA.Fe. a) XRD pattern, b) Raman spectra of SA.Fe. High-resolution XPS spectra of c) Fe 2p, d) N 1s, e)S 2p, f) C 1s. g) The Fe K-edge XANES spectra of SA.Fe and reference samples. h) FT-EXAFS spectra of SA.Fe along with the reference samples. i) EXAFS fitting curve of SA.Fe and FePc. j–l) WT-EXAFS of Fe foil, FePc and SA.Fe at the Fe K-edge. m) PFM voltage intensity of SA.sub. n) PFM voltage intensity and o) PFM voltage phase of SA.Fe.

The sharp increase with Fe-N_4 coupling indicates greater carbon disorder due to disruption of KB's π–π conjugated structure.

XPS and XAFS were used to study the electronic state and coordination environment. The Fe 2p XPS spectra of SA.Fe and cluster Fe (Figure 3c) show Fe species in the forms of Fe-N, Fe^{2+}, and Fe^{3+}. The binding energy of SA.Fe shows a 0.5 eV blue shift compared to cluster Fe, indicating that Fe in SA.Fe is in a more reduced state, supported by lower S content confirmed by XPS elemental analysis and EDS mapping (Table S2, Supporting Information). The N 1s XPS spectra of SA.Fe (Figure 3d) reveals pyridinic nitrogen (398.2 eV), pyrrolic nitrogen (399.1 eV), graphitic nitrogen (401.7 eV), and oxidized nitrogen (403.5 eV). The peak corresponding to pyridinic nitrogen is the most prominent characteristic peak, confirming the defect-rich nature of SA.Fe. The S 2p XPS spectrum of SA.Fe (Figure 3e) shows peaks at 163.3 and 164.8 eV, corresponding to the $2p^{3/2}$ and $2p^{1/2}$ peaks of CSC(N) species. Minor peaks at 167.5 and 169.0 eV are due to oxidized sulfur (CSO_xC). The C 1s spectrum (Figure 3f) shows peaks for C—C═O, C-S, C-N, and C-C structures, with the highest peak for C-C, indicating the KB carbon skeleton. Notably, the absence of Fe-S and Fe-C peaks suggests the single-atom characteristic of Fe in Fe-N_4 couplings. The XPS spectra of SA.sub, pure sub, and cluster Fe are shown in Figures S7–S9 (Supporting Information). SA.sub has similar S and N doping environment as SA.Fe. The pure sub shows a stronger pyrrolic peak, indicating a different N doping structure due to excess CN_x fragments. The weaker S 2p signal in cluster Fe suggests that excessive Fe-N_4 coupling hinders S species hybridization.

The Fe K-edge XANES spectrum of SA.Fe (Figure 3g) shows a lower absorption threshold than Fe foil (Figure S10, Supporting Information), indicating positively charged Fe atoms. This shift confirms the formation of a polar coupling, with nitrogen as the electronegative terminus and iron as the electron-deficient terminus. The FT-EXAFS spectrum (Figure 3h) shows a peak at 1.5 Å, consistent with the Fe-N bond. The absence of a 2.1 Å Fe-Fe bond peak confirms SA.Fe's single-atom characteristics. The bond length of SA.Fe was calculated to be 1.58 Å according to the data fitting result. The calculated Fe-N bond length aligns with FePc, confirming Fe-N_4 coupling coordination (Figure 3i). Wavelet transform (WT)-EXAFS contour plots (Figure 3j–l) show a pronounced peak at 13 $Å^{-1}$ for SA.Fe, corresponding to the Fe-N bond, while iron foil has a peak ≈9.7 $Å^{-1}$.

Piezoelectric force microscopy (PFM) was conducted with a ±10 V bias to study the impact of polar field, which was spontaneously generated by the Fe-N_4 couplings. SA.sub and pure sub showed no characteristic curves (Figure 3m; Figure S11, Supporting Information). In contrast, SA.Fe and cluster Fe displayed a clear ferroelectric hysteresis loop in both amplitude (Figure 3n; Figure S12a, Supporting Information) and phase plots (Figure 3o; Figure S12b, Supporting Information), which confirms the short-range polar electric fields formed by Fe-N_4 coupling. The size of the hysteresis loop opening can be used to evaluate the strength of the internal electric field. Generally, a larger hysteresis loop opening indicates a stronger polarization field, as a higher external voltage is required to overcome it during the reversion of the voltage phase. Herein, before undergoing the electrochemical reactions, cluster Fe exhibits a stronger polar field than SA.Fe due to the abundance in Fe-N_4 coupling, which is verified by the comparison of PFM phase plot (Figure S12c, Supporting Information).

2.3. Electrochemical Performance of SA.Fe in PIBs

The galvanostatic curves (**Figure** 4a) show distinct differences among the materials. The fifth cycle galvanostatic curves (Figure 4b) show decreasing overpotential in the order: pure sub, cluster Fe, SA.sub, SA.Fe. In the 90th cycle galvanostatic curve (Figure 4c), SA.Fe maintains the lowest overpotential after extensive K^+ cycling, while SA.sub shows a significant increase in overpotential. With the polar electric field, SA.Fe and cluster Fe demonstrate a higher retention of the specific capacity. The field significantly improves the K^+ storage efficiency while reducing the reaction overpotential. The result is verified by cyclic voltammetry (CV) curves (Figure 4d). At a scan rate of 0.1 mV s^{-1}, SA.Fe exhibits a stronger Faradaic currents, indicating enhanced K^+ adsorption. The enlarged region in Figure 4e shows SA.Fe with the lowest reduction overpotential. This suggests lower activation energy and improved redox reversibility.

A comprehensive evaluation of SA.Fe, SA.sub, pure sub, and Fe clusters as anode materials forPIBs revealed that SA.Fe, benefiting from the synergistic effects of Fe-N_4 coupling and the polar electric field, exhibited outstanding electrochemical performance. A rapid horizontal electron transfer network is established by and the highly conductive KB substrate, which effectively facilitates the electron transfer efficiency. Vertically, the strong coordination between Fe-N-C induces a spontaneous short-range polar electric field, which provides fast transportation channel that accelerates both ion and electron transportation. Consequently, the affinity for K^+ is enhanced, which results in the outstanding electrochemical performance. Specifically, cycling performance was evaluated at0.1 A g^{-1} (Figure 4f). The SA.Fe electrode stabilized at 444.1 mA h g^{-1} with 99.1% Coulombic efficiency, indicating excellent reaction reversibility. In contrast, SA.sub showed significant capacity decay with a decay rate of 43.3%, showing poorest material integrity. The comparison highlights the critical role of Fe-N_4 coupling in stress regulation. Without Fe-N_4 coupling to regulate electron flow and stress, SA.sub experiences concentrated stress, attributed to the severe volume expansion during potassiation/depotassiation. This leads to the surface cracking and electrode failure. Furthermore, SA.Fe retained a highest reversible capacity of 446.3 mA h g^{-1} and Coulombic efficiency of 99.1% after 100 cycles (Figure 4g). This reflects the superior reaction reversibility and material integrity improved by the polar electric field and strong Fe-N-C coordination, indicating advantages over unregulated carbon materials. Consequently, SA.Fe demonstrates the excellent specific capacity and cycling stability (Figure S13, Supporting Information). To confirm the continuous effect of polar electric field, PFM polarization voltage tests were conducted on the cycled electrode of SA.Fe and cluster Fe (Figure S14, Supporting Information). The hysteresis loops in the voltage phase diagrams show that the Fe-N_4 coupling's polarization electric field remains intact despite repeated potassiation/depotassiation.

In high current density performance, SA.Fe exhibited an excellent cycling performance at 2 A g^{-1} (Figure 4h), stabilizing at 192.2 mA h g^{-1} after 3000 activation cycles. With a minimal

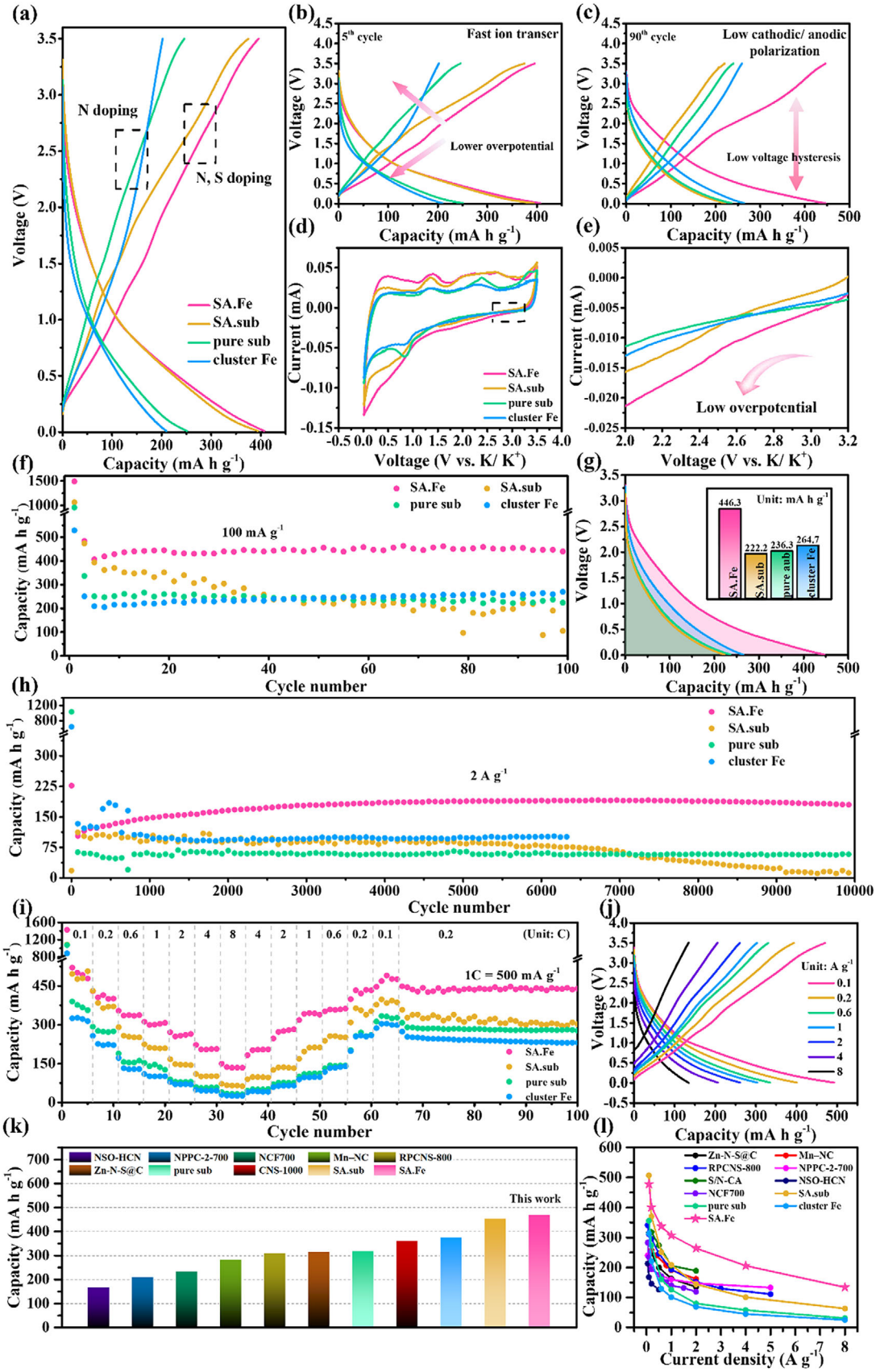

capacity loss of 0.00082% per cycle over the next 7000 cycles. SA.Fe maintained 180.6 mA h g^{-1} and ≈100% Coulombic efficiency after 10 000 cycles. This exceptional stability highlights the stress regulation from Fe-N_4 coupling and the polarization electric field. Also, SA.Fe exhibited excellent rate performance at current densities from 0.1 to 10 A g^{-1} (Figure 4i), maintaining higher capacity and retention. It delivered capacities of 479 to 134 mA h g^{-1} across increasing current densities and retained 448 mA h g^{-1} with 98.8% Coulombic efficiency upon returning to 0.2 A g^{-1}. This can be attributed to the higher capacitance contribution resulted from the polar electric field. The efficient K^+ adsorption enables SA.Fe to maintain a high specific capacity under high current density. Galvanostatic profiles (Figure 4j) confirmed consistent K^+ adsorption across varying current densities.

K^+ storage capacity comparisons (Figure 4k) underscore the superiority of SA.Fe over the reported carbon-based materials.[39,46,51–55] The previously studied material consists of different carbon substrate, such as GO, graphene, graphite, all of which exhibit a relatively low specific capacity of less than 300 mAh g^{-1}. In contrast, all of the materials in this study outperform the reported carbonaceous materials. The result indicates that the KB substrate provides an excellent coordination environment and efficient electron transport pathways. This serves as a robust foundation for the holistic regulation of K^+ by Fe-N_4 coupling. Moreover, SA.Fe, with its polar electric field, showed an absolute advantage in the comparisons. The performance gap became even more pronounced in the rate capability comparison (Figure 4l). SA.Fe exhibited exceptional rate capability. The comparison confirms the reinforced K^+ adsorption and the accelerated kinetics attributed to the polar field. This establishes SA.Fe as the superior performer among currently studied carbonaceous anodes.

2.4. Electrochemical Property and K^+ Kinetics Evaluation

Cyclic voltammetry (CV) curves at varying scan rates (0.1–1.0 mV s^{-1}) were used to analyze the K^+ storage mechanism and quantify capacitive and diffusive contributions (**Figure 5a**). In the first cycle, prominent peaks at 1.5 and 2.5 V in the reduction profile indicate SEI layer formation and sulfur derivative reactions, which disappears in the following cycles. As shown in the following cycles, the peaks at 0.61 and 0.01 V correspond to K^+ adsorption at nitrogen sites and carbon intercalation, confirming the combined K^+ storage mechanism of intercalation and adsorption. This can be verified through the QV curves of SA.Fe (Figure S13, Supporting Information). SA.Fe demonstrates a smooth curve in the voltage span of 0.01–3 V, which differs from the flat voltage plateau at a low potential offered by the common seen carbon-based materials, such as graphite. A smoother curve is observed below 1 V, corresponding to the K^+ adsorption reaction provided by the Fe-N_4 couplings. In contrast, a pronounced voltage plateau appears in the range of 0.01–0.5 V, indicating the contribution of K^+ intercalation. Within the voltage range, both K^+ intercalation and adsorption significantly contribute to the overall capacity, hence demonstrates a broader voltage plateau. These results indicates that the Fe-N_4 couplings provides the additional active stie for the K^+ adsorption, while the durable KB substrate remains the K^+ storage ability driven by intercalation. The additional adsorption active site accelerates the K^+ reaction kinetics, but also contributes to the extra specific capacity. The combined mechanism can be further validated by the following theoretical-specific calculation in the DFT simulation section.

The high consistency of the CV curves demonstrates SA.Fe's excellent reaction reversibility. According to calculated result of Randles–Sevick equation. The b values for SA.Fe consistently exceeds 0.75 (Figure 5b), confirming its capacitive adsorption nature. The results further quantify the capacitive and diffusion-controlled contributions based on area ratios. At a scan rate of 0.4 mV s^{-1}, SA.Fe's capacitive contribution is 56.3% (Figure 5c), while SA.sub and cluster Fe show 46.8% and 65.8%, respectively (Figure S15, Supporting Information). The Fe-N_4 coupling notably boosts the capacitive ratio, as the polarization electric field effectively enhances K^+ adsorption. At a scan rate of 0.2 mV s^{-1}, SA.Fe shows a 50.1% capacitive contribution (Figure 5c). This balance between capacitive and diffusion control aligns with DFT simulations of adsorption energy and diffusion barriers, confirming that Fe-N_4 coupling enhances K^+ diffusion through effective electron regulation.

Moreover, the K^+ diffusion kinetics of various electrodes were further investigated by the galvanostatic intermittent titration technique (GITT), as illustrated in Figure 5d,e. The diffusion coefficient (D) of SA.Fe is calculated, ranging from 2.6×10^{-9} to 3.9×10^{-9}, shows a 32–68% increase compared to other materials, indicating superior K^+ diffusion. The increased diffusion coefficient corresponds to the lowest diffusion energy barrier observed in DFT simulations. In-situ Nyquist plot is established by the electrochemical impedance spectroscopy (EIS) (Figure 5f) displays a high-frequency semicircle and low-frequency line during the initial cycle, indicating SEI formation. Impedance rises during charging, verifying K^+ adsorption in SA.Fe. Further analysis of the Nyquist plot during charging and discharging (Figure S16a,b, Supporting Information) reveals that SA.Fe demonstrates a clear advantage over all other materials. Regardless of the state, SA.Fe exhibits significantly lower impedance, ≈1500 Ohm, while the impedance of other materials exceeds 2000 Ohm. This improvement is attributed to the formation of a higher-quality SEI layer. Through effective electron regulation, SA.Fe enhances the reaction kinetics at the electrode-electrolyte interface, leading to more efficient SEI layer formation. A stable SEI layer contributes to maintaining material integrity and facilitates rapid ion and electron transport, laying a solid foundation for SA.Fe's superior long-cycle performance. These findings align with results from LSV and other electrochemical tests,

Figure 4. Electrochemical performance as PIB anodes in a half-cell configuration. a) Galvanostatic profile of SA.Fe, SA.sub, pure sub, cluster Fe. The corresponding galvanostatic profile at b) 5th and c) 90th cycle, respectively. d) The CV curves of the electrode at a scan rate of 0.1 mV s^{-1} and e) the magnification of the selected area. f) Cycling performance of all the samples at 0.1 A g^{-1} over 100 cycles. g) The comparison of Specific capacity at 0.1 A g^{-1} over 100 cycles. h) Long-term cycling performance of all the samples at 2 A g^{-1}. i) Rate performances of all samples at various current densities. j) Galvanostatic charge/discharge curves of SA.Fe at different current density. Comparison of the rate performance with reported carbonaceous materials for PIB anodes at k) the current density of 0.1 A g^{-1} and l) the various current density ranging from 0.1 to 8 A g^{-1}.

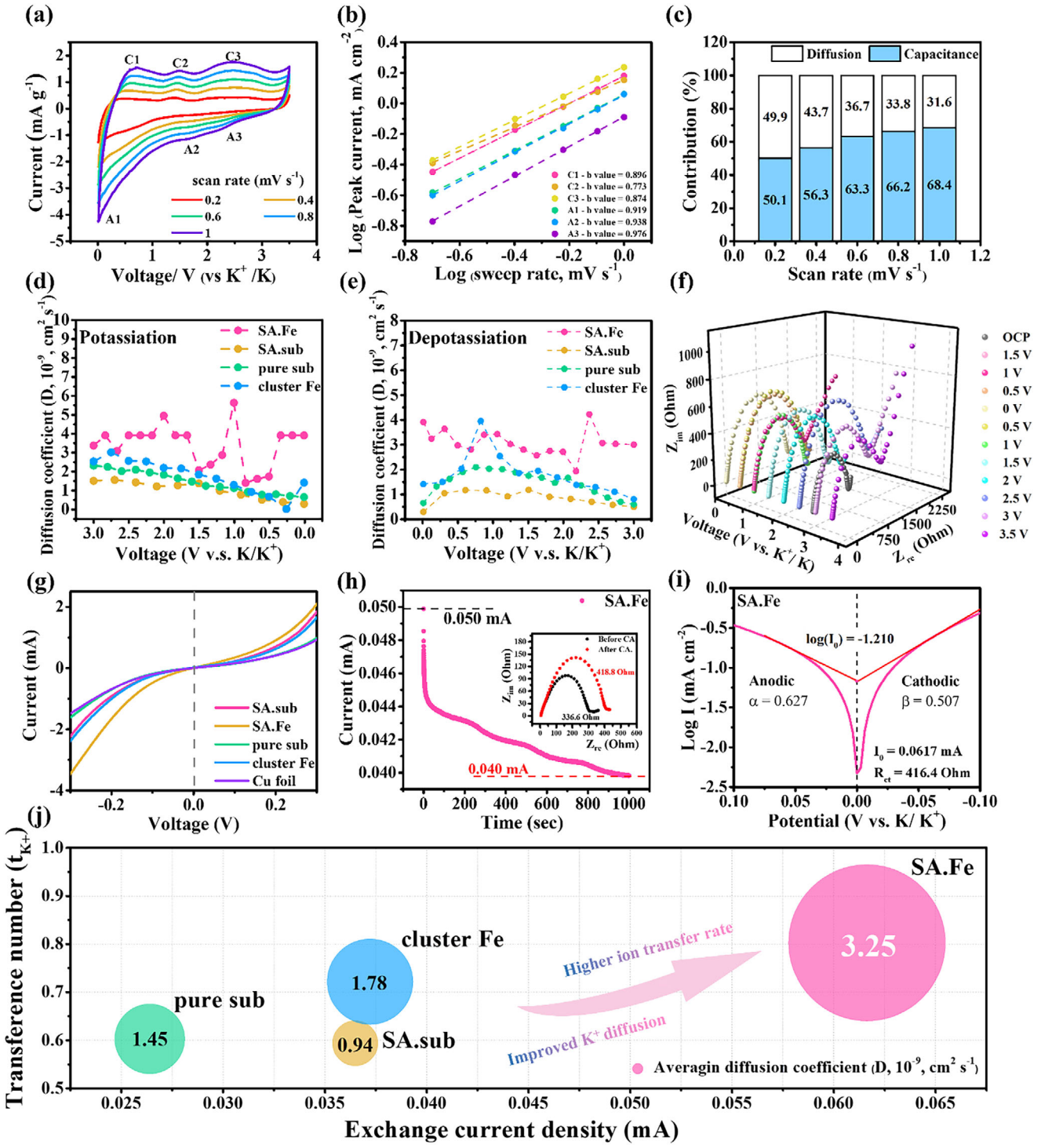

Figure 5. Electrochemical property and K^+ kinetics evaluation. a) CV curves of SA.Fe at various scan rates ranging from 0.2 to 1 mV s^{-1}. b) b value and c) the capacitive contribution in SA.Fe at different scan rates. GITT potential profiles of SA.Fe in d) depotassiation and e) potassiation process. f) The in-situ Nyquist plots of SA.Fe. g) Linear sweep voltammetry (LSV) of SA.Fe. h) The profile chronoamperometry (CA) and the corresponding Nyquist plot of SA.Fe for the calculation of transference number (t_{K+}). i) Detailed Tafel calculation of SA.Fe. j) The comprehensive comparison of the K^+ kinetics and the K^+ diffusion.

confirming that the Fe-N_4 coupling and the resulting polar field play a pivotal role in improving reaction kinetics.

To understand the impact of SA.Fe's polarization electric field on electron and K^+ migration, electron transfer efficiency was evaluated via LSV and transference number (t_{K+}). Pure copper electrodes served as benchmarks to evaluate the impact of surface modifications on reaction kinetics. Figure 5g and Figure S17 (Supporting Information) illustrate the linear sweep voltammetry (LSV) scanning results and the corresponding Tafel curves, respectively. SA.Fe demonstrates a notably higher current density slope in the LSV characteristic curves, reflecting enhanced K^+ migration efficiency at the electrode interface. Linear fitting in the mixed control region (≈50 mV) was used to determine the anodic Tafel slope (α), cathodic slope (β), and exchange current density (i_0). SA.Fe shows charge transfer coefficients α and β of 0.627 and 0.507, respectively, with an exchange current density of 0.062 mA cm^{-2} (Figure 5i). With the Fe-N_4 coupling's polarization electric field, K^+ were strongly attracted from the electrolyte. This accelerates the migration to the electrode surface and reduces concentration polarization, confirming improved reaction kinetics in SA.Fe.

In contrast, SA.sub, cluster Fe, pure sub, and Cu foil exhibit significantly lower charge transfer coefficients and exchange current densities (Figure S18, Supporting Information). Notably, cluster Fe's higher electron exchange density underscores the benefits of Fe-N_4 coupling and the polarization electric field in enhancing electron exchange and K^+ mass transfer. Cu shows a higher exchange current density than pure sub due to its superior conductivity. Charge transfer resistance (R_{ct}) at the electrode interface was calculated by the Tafel equation. The lower resistances in SA.Fe and cluster Fe confirm the conductivity boost from Fe-N_4 coupling. Moreover, SA.sub's lower resistance compared to pure sub indicates sulfur doping also improves conductivity through electron regulation. To evaluate charge transfer efficiency, the t_{K+} number[56–59] was measured at 20 mV (purely electronic control region) to isolate K^+ mass transfer effects. Using chronoamperometry (CA) and EIS, the t_{K+} number was calculated by the formula:

$$t_{K+} = \frac{I_s\left(\Delta V - I_0 R_0\right)}{I_0\left(\Delta V - I_s R_s\right)} \quad (1)$$

where ΔV is the applied polarization voltage (20 mV), I_0 and I_s are the initial and steady-state currents, R_0 and R_s are the initial and steady-state impedances obtained by EIS. The t_{K+} numbers for SA.Fe, SA.sub, pure sub, cluster Fe, and Cu are 0.802, 0.593, 0.602, 0.721, and 0.736, respectively (Figure 5h; Figure S19 and Table S3, Supporting Information). Thehighestvalue of SA.Fe highlights its excellent charge transfer efficiency. While Cu exhibits high t_{K+}, its low exchange current density in LSV reveals limited K^+ mass transfer, caused by insufficient active adsorption sites, which hinders its overall kinetic performance. This emphasizes the crucial role of the polarization electric field in improving both K^+ adsorption and mass transfer. With the added advantage of the conductive KB substrate, SA.Fe shows superior K^+ kinetics and enhanced diffusion (Figure 5j).

2.5. K^+ Storage Mechanism of SA.Fe and DFT Simulations

Ex-situ XPS spectra (**Figure 6a–e**) were analyzed to examine energy changes during potassium insertion/extraction in SA.Fe. Periodic shifts in the K 2p XPS spectra indicate dynamic electron transfer and bond formation during K^+ insertion/extraction. During discharge, distinct energy peaks at points b and d reflect the formation of the weak K-C, K-N, and K-S bonds. In the second cycle, the K 2p spectra exhibit a positive shift during discharge/potassiation and a negative shift during charge/depotassiation, confirming reversible K^+ storage mechanism. The N and S active sites show similar energy changes. The N 1s spectra primarily features pyridinic nitrogen, while the S 2p spectra reveal peaks for thiophene-type sulfur near the Fe-N_4 coupling. During potassiation (points a to b and c to d), K^+ donate electrons, forming weak coordination bonds with sulfur and nitrogen, leading to slight negative energy shifts in both N 1s and S 2p spectra. These peaks shifts back to the pristine binding energy during depotassiation (point b to c and d to h), indicating the reverse electron transfer. The result signifies an excellent reversibility during the cycle, resulting in the outstanding cycling performance. As shown in the Fe 2p spectra, Fe sites store charges and show a slightly downward-shifted energy peaks during potassiation, while electron-rich N anions provide additional K^+ storage sites. During depotassiation, both charge and K^+ are released, and energy peaks return to their pristine levels. The result indicate that single-atom Fe sites serve as charge storage carriers, absorbing excess electrons from adjacent N or S sites. This electron absorption enhances charge transfer, modulates bond strength, and improves K^+ adsorption performance.

Density functional theory (DFT) calculations were performed to analyze the electronic structure. Based on XPS, XAS, EDS mapping and other elemental analyses, we established the following four molecular models through DFT optimization, as shown in Figure S20 (Supporting Information). Specifically, the model of cluster Fe is simplified due to the side reaction of the stacking Fe-N_x fragments, which only occurs in the early stage, then disappear in the following cycle. This is verified by the electrochemical measurements (Figure 4f,h) and the comparison of STEM images (Figure S21, Supporting Information) with a detailed explanation. In SA.sub and pure sub, lacking Fe-N_4 coupling, a higher total density of states (TDOS) was observed (Figure 6f), due to the fully conjugated π-π KB matrix. The continuous TDOS at the Fermi level indicates excellent electrical conductivity of the KB substrate. On the other hand, in SA.Fe, Fe-N_4 coupling causes hybridization in the KB network, disrupting π-π conjugation and slightly reducing TDOS. However, the continuous TDOS near the Fermi level shows that Fe-N_4 coupling preserves KB's electron transport capabilities. In contrast, cluster Fe, without sulfur doping, shows a discontinuous energy gap near the Fermi level, highlighting sulfur's key role in regulating electron transport.

The overlapping DOS of Fe, S, and N at the Fermi level in SA.Fe indicates a strong coordination environment that supports material integrity. The alignment of Fe's DOS with the Fermi level enhances orbital overlap, according to Nørskov's D-band center theory, improving K^+ kinetics.[60–62] The strong localization of d-electrons also ensures stable electron transfer during potassiation and depotassiation. The Electron Localization

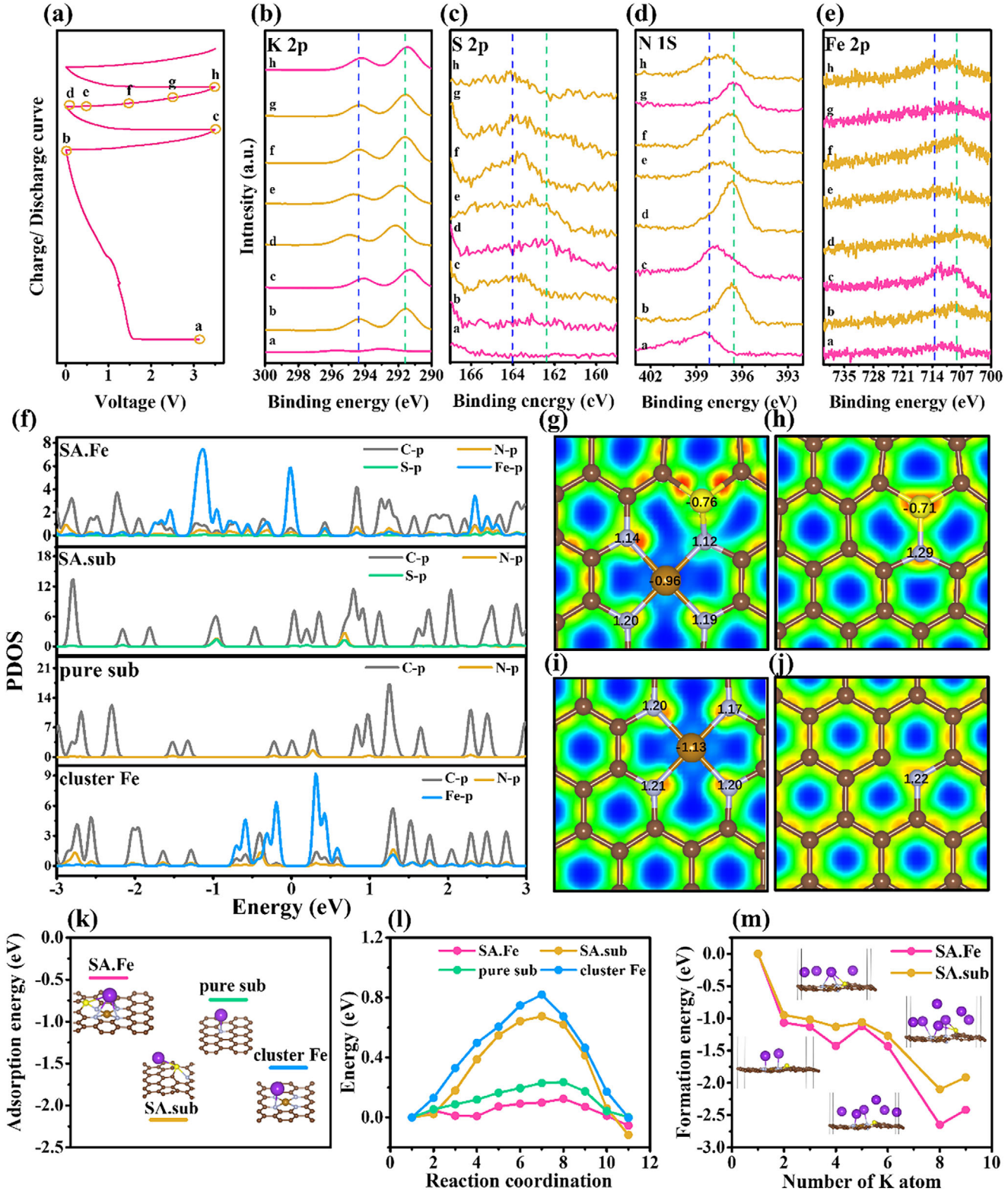

Figure 6. K^+ storage mechanism of SA.Fe and DFT simulations. a) Discharge and charge process of the sample preparation for ex-situ XPS measurements b) K 2p c) N 1S d) S 2p e) Fe 2p ex-situ XPS spectra of SA.Fe. f) Partial density of states (PDOS) of SA.Fe, SA.sub, pure sub, and cluster Fe. Electron localization function (ELF) of g) SA.Fe, h) SA.sub, i) pure sub, and j) cluster Fe. k) Adsorption energy (E_{ad}) of K^+ on SA.Fe and SA.sub. l) Energy barriers for K^+ diffusion along the minimum energy path over SA.Fe, SA.sub, pure sub, and cluster Fe. m) Formation energy (E_f) as a function of the number of K^+ for SA.Fe and SA.sub electrodes.

Function (ELF) plots (Figure 6g–j) show distinct electron distribution differences due to Fe-N_4 coupling. This contributes to the polar field formation discussed in the PFM measurements (Figure 4n,o), which plays the important role in the holistic electron and ion regulation. In N-doped (pure sub) and S and N-doped (SA.sub) systems without Fe-N_4 coupling, electron localization remains largely unchanged. In contrast, SA.Fe and cluster Fe display significant electron distribution shifts between Fe and adjacent N sites, consistent with ex-situ XPS electron transfer observations. In SA.Fe, Fe attracts electrons from the carbon matrix toward the N site, creating a strong Fe-N_4 interaction. This is supported by the localized electron density at the Fe site, aligning with the D-band center theory. In contrast, cluster Fe shows reduced electron localization at the Fe center due to the presence of sulfur, highlighting sulfur's role in electron regulation. The electron localization differences between N and Fe in SA.Fe arise from their significant electronegativity difference, creating polarized covalent bonds and increasing electron density at the N site. This enhanced electron density improves K^+ affinity and adsorption, consistent with TDOS observations.

The adsorption energy (Figure 6k) indicates K^+ affinity While Fe-N_4 coupling strongly attracts K^+, Fe sites absorb excess electrons from the N site via Fe d orbitals, weakening K-N bond polarization and lowering adsorption energy, which facilitates K^+ migration to other sites. Consequently, SA.Fe exhibits the lowest adsorption energy, further reduced by S dopants. SA.Fe's moderate adsorption energy results in a significantly lower K^+ migration energy barrier. As shown in Figure 6l, SA.Fe has the lowest diffusion energy barrier, highlighting its superior K^+ diffusion capability. Diffusion pathways are shown in Figure S22 (Supporting Information). K^+ adsorption ability was evaluated through formation energy calculations (Figure 6m), with detailed models in Figure S23 (Supporting Information). SA.Fe shows lower formation energies than SA.sub. All the results highlight that Fe-N_4 couplings provide the holistic regulation in both K^+ diffusion and K^+ adsorption, leading to a well-balanced kinetic performance. Based on the calculated K^+ adsorption behavior of SA.Fe (Figure S23a, Supporting Information), the material exhibits the most stable adsorption structure when six K^+ are adsorbed. The Fe-N_4 polar couplings anchored on the KB substrate provide the additional adsorption site for K^+ storage. Hence, the specific capacity is enhanced.

2.6. K^+ Concentration Distribution and Stress Dispersion Mechanism

As shown in the electrochemical performance, cluster Fe exhibited a significant specific capacity degradation, while SA.Fe maintain a steady charging/discharging curves over 10 000 cycles. Additionally, the weakening of the polar electric field in cluster Fe was observed by the voltage hysteresis loop comparison between the cycled SA.Fe and cluster Fe. These results indicate that the weakening polar field, attributed to the collapse of Fe-N_4 couplings, lead to the specific capacity degradation. Hence, Finite element analysis (FEA) is conducted to study the stress-induced Fe-N_4 coupling degradation during potassiation/depotassiation process.

FEA simulated K^+ concentration and stress distribution after potassiation. In the cluster Fe model, strong π–π interactions hindered the optimal decomposition of Fe-N_x, causing surface aggregation due to van der Waals forces. The model features a broad rectangular region for the KB substrate and smaller rectangles for uniformly distributed S-doped Fe-N_4 coupling. Two-layered rectangular regions represent Fe-N_x stacking in cluster Fe. SA.Fe and cluster Fe are depicted with 5×5 and 7×7 coupling unit matrices, respectively, to highlight differences in Fe-N_4 coupling density. Detailed models are provided in Figure S24 (Supporting Information). **Figure** 7a shows the K^+ concentration profile from FEA. Post-potassiation, SA.Fe exhibits uniform K^+ adsorption with no concentrated areas. Conversely, cluster Fe (Figure 7d) displays high K^+ concentration around active sites, forming a radial gradient and indicating uneven distribution. This irregular K^+ adsorption in cluster Fe is likely due to densely packed Fe-N_4 couplings, which impede K^+ diffusion. This is supported by diffusion energy barrier simulations, confirming that excessive coupling aggregation disrupts uniform K^+ adsorption and diffusion.

Stress distribution simulations based on K^+ concentration reveal that SA.Fe maintains a uniform stress distribution, enduring $\approx 1.7 \times 10^4$ Pa at the Fe-N_xS/KB interface (Figure 7b). In contrast, cluster Fe experiences high-stress concentration of up to 3.1×10^4 Pa due to its stacked structure (Figure 7e). The concentrated stress within the material may cause the deformation, eventually lead to the collapse and loss of the top Fe-N_x fragments and the underlying Fe-N_4 couplings. This weakens the polar field originates from the couplings, thereby hindered the K^+ adsorption and the reaction kinetics in cluster Fe, consequently, showing a decay in the specific capacity. Uniform K^+ adsorption helps modulate stress distribution, further improves the material integrity and the cycling performance. The result emphasizes the crucial role of well-distributed Fe-N_4 coupling in stress regulation. SEM images (Figure 7c,f) show that SA.Fe maintains integrity with minimal cracking, while cluster Fe exhibits significant cracking after 100 cycles. FEA stress distribution findings reveal that stress concentration in stacked structures leads to cracking and reduced material integrity. SEM images of pure sub and SA.sub electrodes also show severe cracking after 100 cycles (Figure S25, Supporting Information). Pure sub shows severe cracking up to 15 µm due to lack of Fe-N_4 coupling, leading to concentrated stress and poor integrity. This highlights Fe-N_4 coupling's role in stress regulation, as Raman spectra indicate improved stress tolerance in Fe-N_xS/KB. Figure 7g shows that SA.Fe has uniform stress with a maximum of 1.8×10^4 Pa, whereas cluster Fe has concentrated stress of 2.7×10^4 Pa, likely causing material expansion from K^+ adsorption. After 100 cycles with the electrolyte of 4 M KFSI DME, ex-situ SEM images reveal that post-potassiation thicknesses are 15.8 µm for SA.Fe and 28.5 µm for cluster Fe (Figure 7h,i). SA.Fe and cluster Fe expand by 44% and 50%, respectively, with the greater expansion in cluster Fe attributed to concentrated stress in its unit. To verify the experimental result, the ex-situ SEM images of the electrode cycled with the electrolyte of 1 M ᴍKFSI DME were taken (Figure S26, Supporting Information). Table S4 (Supporting Information) details the volume expansion rate calculation and comparison, confirming that non-uniform stress distribution leads to significant electrode expansion, compromising integrity and causing failure.

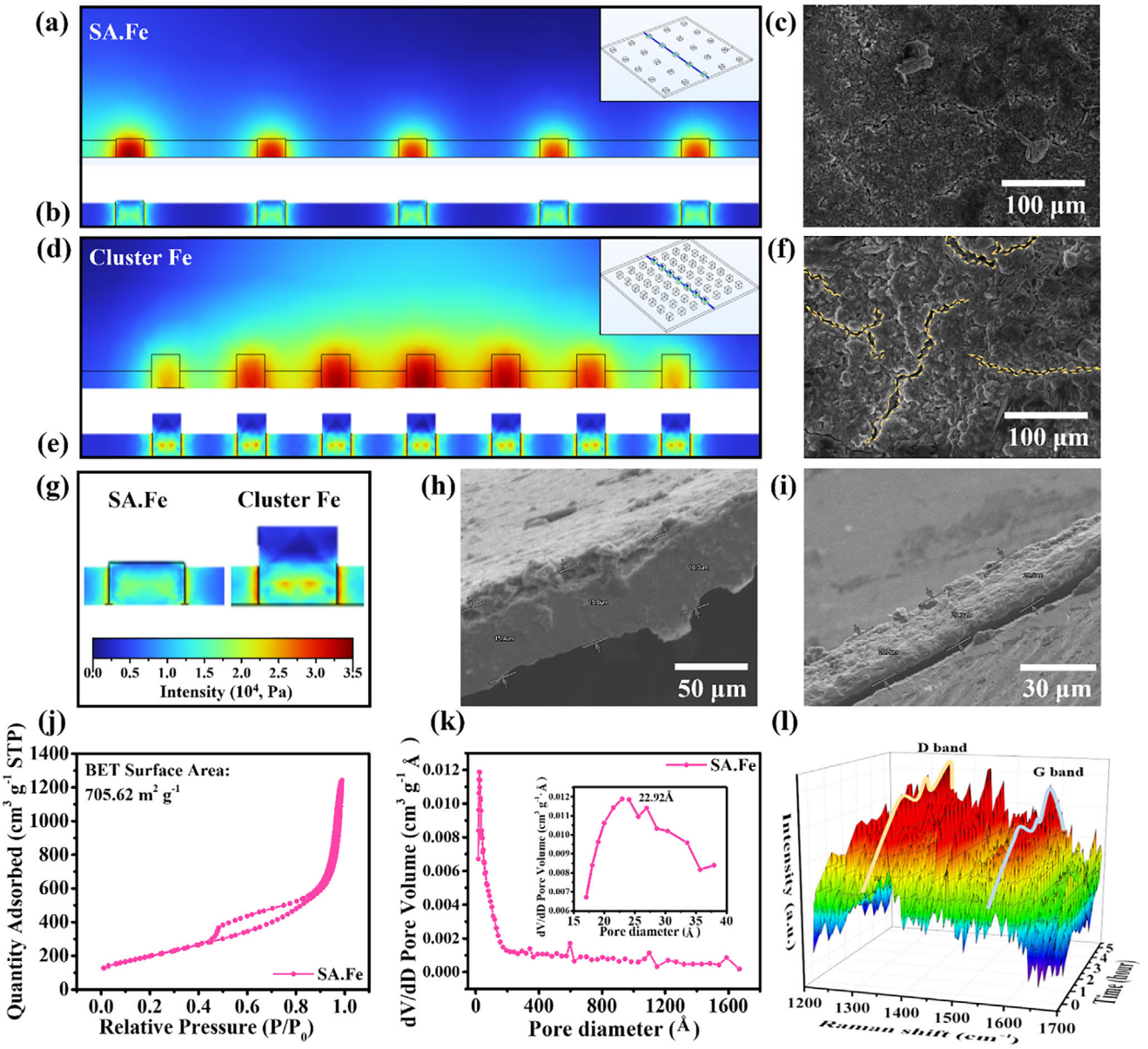

Figure 7. K^+ concentration distribution and stress dispersion mechanism. The corresponding potassium concentration of a) SA.Fe and d) cluster Fe in FEA simulations. Stress distribution of b) SA.Fe and e) cluster Fe in FEA simulations. The cycled electrode surface SEM images of c) SA.Fe and f) cluster Fe. g) Comparison of stress distribution between SA.Fe and cluster Fe. SEM images of the thickness comparison between h) SA.Fe and i) cluster Fe after 100 cycles in the electrolyte of 4 M KFSI DME. j) Nitrogen adsorption–desorption isotherms, k) pore size distribution, and the l) in-situ Raman spectra of SA.Fe.

Nitrogen adsorption-desorption isotherms (Figure 7j) show that SA.Fe has a large specific surface area of 705.62 m^2 g^{-1} due to the porous KB substrate. Particle size distribution (Figure 7k) indicates microporous structures measuring 22.92 Å (pristine KB) and 26.94 Å (Fe-N_xS/KB hybrid), which help buffer stress during potassiation/depotassiation, enhancing SA.Fe's stress tolerance. In-situ Raman spectra (Figure 7l) reveal changes in D-band and G-band intensity, with the I_D/I_G ratio increasing from 1.14 to 1.19 during potassiation and returning to 1.16 during depotassiation, indicating high reversibility.

2.7. Electrochemical Performance of SA.Fe in PMBs

The enhances K^+ storage performance, reaction kinetics, and significantly benefits metal deposition processes in PMBs. The polarization electric field is crucial for reducing nucleation overpotential during deposition, leading to a more uniform coating process. This extends the cycling life of potassium metal batteries by enhancing electrode stability and longevity. The reversibility and stability of the materials were assessed using asymmetric cells cycled at 0.5 mA cm^{-2} with a capacity of 0.5 mA h cm^{-2} (**Figure 8a**). Pure sub and SA.sub failed after 425 h, while

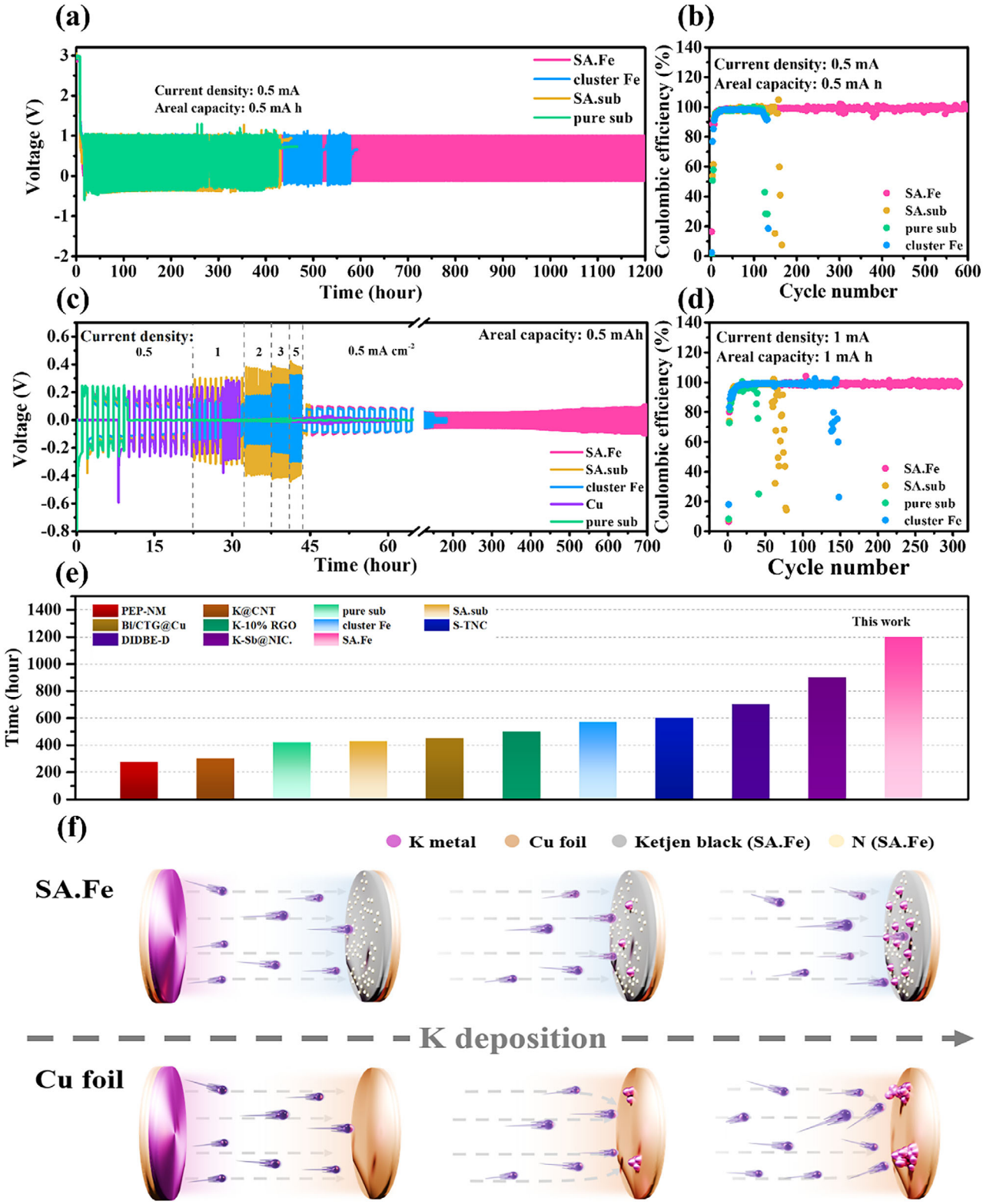

Figure 8. Electrochemical performance as PMB anodes in a half-cell configuration. a) Cycle stability of the asymmetric cells at 0.5 mA cm^{-2} with a fixed areal capacity of 0.5 mA h cm^{-2}, and the corresponding b) Coulombic efficiency. c) Voltage profiles of the asymmetric cells at various current densities under a fixed areal capacity of 0.5 mA h cm^{-2}. d) The corresponding Coulombic efficiency of the asymmetric cells at 1 mA cm^{-2} with a fixed areal capacity of 1 mA h cm^{-2}. e) Comparison of the rate performance with reported carbonaceous materials for PMB anodes at the current density of 0.5 mA cm^{-2} and areal capacity of 0.5 mAh cm^{-2}. f) The schematic illustration of dendrite formation mechanism.

cluster Fe, despite a relatively longer cycling life, showed significant voltage fluctuations and failed after 600 h. The Coulombic efficiency plot (Figure 8b) confirms this, with a sharp decline in efficiency after ≈150 cycles, indicating voltage failure. In contrast, SA.Fe demonstrated outstanding durability and stability, achieving 1200 h of cycling life (600 cycles). The stable voltage profile in the time-voltage plot reflects a consistent coating/stripping process. Finally, SA.Fe showed the lowest nucleation overpotential (Figure S27, Supporting Information), indicating more efficient and uniform K metal deposition. This improvement is due to the polarization electric field from Fe-N_4 coupling, which enhances uniform deposition and reduces overpotential.

Furthermore, when the current density was increased to 1 mA cm^{-2} with a capacity of 1 mA h cm^{-2} (Figure 8d), SA.Fe maintained a reversible stripping/coating process and stable Coulombic efficiency for 900 h (300 cycles). Detailed voltage profiles are shown in Figure S28 (Supporting Information). In contrast, other materials failed within 50–150 h. SA.Fe's performance, showing a 52% to 87% increase in cycling life, suggests that the polarization electric field remains effective at high current densities, improving K metal deposition uniformity and significantly suppressing dendrite formation. Importantly, the advantage of the polar field is further amplified in the rate capability (Figure 8c). After undergoing current density variations of 0.5, 1, 2, 3, and 5 mA cm^{-2}, materials lacking polar field regulation exhibited short-circuiting, while cluster Fe and SA.Fe demonstrated significantly longer cycle lifespans. Specifically, SA.Fe maintained a lifespan of 700 h even under high current densities. These results confirm the dendrite suppression effect of the polar field, consistent with previous findings. Benefiting from the Fe-N_4 couplings and the polar field, SA.Fe demonstrates exceptional cycling stability, outperforming recently reported carbonaceous materials (Figure 8e).[31,63–68] Most of the reported carbon-based materials lack the regulation of polar electric fields, which limits their ability to enhance the uniformity of K^+ deposition. Carbon-based substrates such as CNT, RGO, and NIC exhibit lower conductivity compared to KB, restricting electron transport and further hindering the uniform deposition of K metal. Additionally, materials with spontaneously generated polar fields, such as cluster Fe and SA.Fe, generally displays superior cycling performance. After coordination adjustments of Fe-N_4 couplings, SA.Fe achieves a stable polar field, further improving its cycling lifespan. This confirms the effectiveness of the polar field in suppressing dendrite formation and significantly enhancing the performance of PMBs.

The advantages of the polar field regulation are illustrated in Figure 8f. The polar field provides the effective directing effect that contributes to the uniform and smooth K metal coating layer, while surface without the polar field regulation forms a concentrated area during the K metal deposition. This affects the distribution of electric field, leading to the non-uniform deposition on the protruding surface, eventually resulting in the formation of dendrite. The directing effect of polar field is verified with the following optical microscope (OM) inspection and the simulations.

To verify the dendrite suppression effect of the polar field with the thick K metal coating on the electrode, EIS, LSV, Tafel, and transference number experiments were performed after the K coating process. Potassium metal layers were formed on the materials under identical discharge conditions (0.5 mA cm^{-2}, 0.5 mA h cm^{-2}). The voltage profiles during the deposition process, are shown in Figure S29a (Supporting Information). The EIS results in Figure S29b (Supporting Information) reveal that SA.Fe exhibits the lowest impedance, providing preliminary evidence of a stable, low-impedance interface contributed by the first uniform metal layer. To analyze the combined effects of electron transfer and K^+ mass transport in the electrolyte, LSV measurements were conducted (Figure S29c, Supporting Information). Tafel curves derived from LSV curve (Figure S29d, Supporting Information) show that SA.Fe and cluster Fe exhibit larger slopes, indicating enhanced K^+ reaction kinetics. Detailed Tafel analysis is shown in Figure S30a–d (Supporting Information). The corresponding calculations significantly higher exchange current densities for SA.Fe and cluster Fe compared to pure sub and SA.sub (Figure S30e, Supporting Information), confirming more efficient K^+ diffusion and reduced concentration polarization in the electrolyte. Additionally, the t_{K+} number is calculated (Figure S31a–d, Supporting Information) to examine the pure electron transfer behavior under multi-layer metal deposition. As shown in Figure S31e (Supporting Information), the t_{K+} number are similar across all materials, indicating no significant enhancement in electron transfer. This can be attributed to the dominant role of potassium metal in thicker coatings, overshadowing the contribution of the underlying material.

In conclusion, the experiments demonstrate that the polar field's effect on enhancing electron transfer is weakened under multi-layer potassium metal deposition, as evidenced by similar t_{K+} number. On the other hand, SA.Fe and cluster Fe with polar fields exhibit larger Tafel slopes and higher exchange current densities due to improved K^+ mass transport in the electrolyte. These results indicate that even under multi-layer deposition, the polar field can still effectively guides K^+, enhancing reaction kinetics. The field is thus verified to benefit the long-term cycling stability and effective dendrite suppression.

2.8. The Mechanism of Dendrite Growth

In-situ imaging of electrode surfaces at 0.3 mA cm^{-2} (**Figure 9a** for SA.Fe and Figure 9c for copper foil) demonstrates that K metal deposition is significantly slower on SA.Fe than on copper foil. After 12 min, SA.Fe shows only a thin K metal coating, while copper foil has a much thicker coating with early signs of dendrite formation. During K metal deposition, nucleation and growth on copper foil disrupt the electric field, accelerating deposition on protruding areas and leading to uneven coating and dendrite formation. In contrast, SA.Fe maintains a uniform K metal deposition process even with protruding metal layers, demonstrating superior control and stability. This uniformity indicates that the polarization electric field effectively mitigates uneven electric fields, ensuring consistent deposition across the material surface. Broader in-situ imaging of SA.Fe (Figure S32, Supporting Information) confirms this, showing a large, flat surface with uniform K metal deposition over an extensive area. The result further indicates the different deposition behavior between SA.Fe and Cu foil.

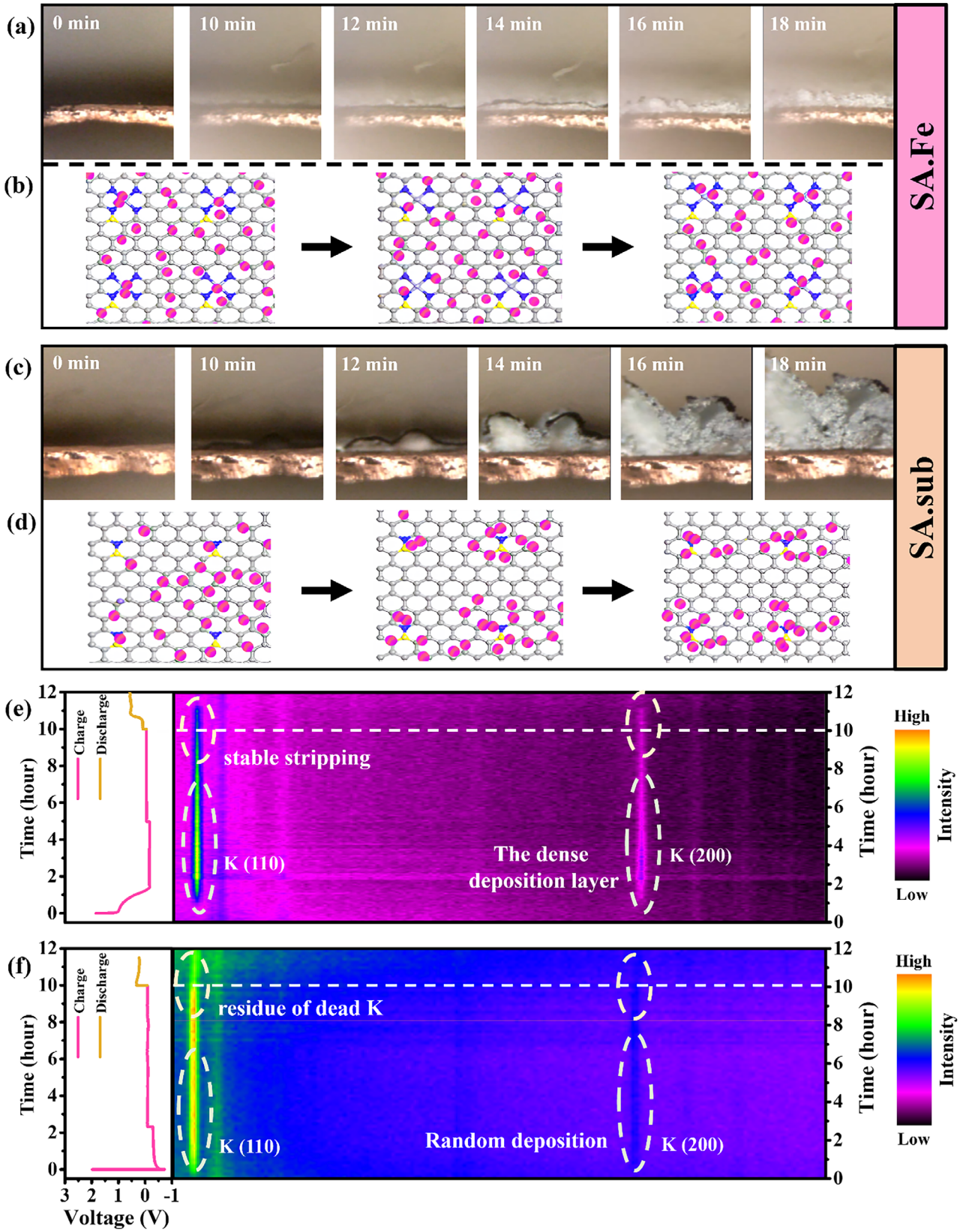

Figure 9. The mechanism of dendrite growth. Operando OM observation of K plating on a) SA.Fe and c) Cu fol. Snapshots of molecular dynamic (MD) simulations of b) SA.Fe and d)SA.sub. In-situ XRD pattern of e) SA.Fe and f) Al foil.

The consistent deposition highlights the polarization electric field's effectiveness in suppressing dendrite formation and validating its role in ensuring uniform coating and stripping processes.

On a macroscopic scale, SA.Fe shows uniform K metal deposition. To explore the molecular mechanisms, kinetic simulations of K^+ diffusion were performed for SA.Fe and SA.sub (Figure 9b,d).[69] During the discharging process, K^+ reduce to K atom and deposit on the material surface. Hence, the K^+ diffusion process can be indicated by the distribution of K atoms. The visual representation of K atom has been magnified and enhanced for clarity, with original simulation results shown in Figure S33 (Supporting Information). Initially, both SA.Fe and SA.sub show uniform K atom distribution. In the early stage, K^+ starts migrating toward active sites and reduces to K atoms on SA.sub, while it remains evenly distributed in SA.Fe. As time goes by, K atom aggregation on SA.sub intensifies around active sites, indicating dendrite formation. In contrast, SA.Fe maintains a uniform K atom distribution, effectively suppressing dendrite formation. Furthermore, K atoms surround the N active sites in SA.Fe more densely than the S sites, indicating that N species primarily serve as adsorption sites for K^+, with S playing a secondary role. This observation is consistent DFT simulations and electrochemical capacitive contribution calculations. Figure S34 (Supporting Information) quantifies K atom clusters with a coordination number greater than 3. Within the early stage, the number of K atom clusters rapidly increases to 20 in SA.sub, while SA.Fe shows a slower increase. This quantification aligns with the observed cycling life, confirming the superior dendrite suppression effect of Fe-N_4 coupling. Katom aggregation is driven by thermodynamic factors, with small K particles tending to cluster to minimize surface energy, increasing dendrite formation risk. However, the polarization electric field from Fe-N_4 coupling aids in capturing K^+ and restricts their free movement. The restricted K^+ then reduces to the uniformly distributed K atoms, further minimizing the formation of K atom cluster.

To evaluate K metal coating/stripping processes, in-situ XRD was performed for SA.Fe and Al foil at 0.5 mA cm^{-2}, with Al foil used as the current collector to reduce interference from Cu XRD signals (Figure 9e,f). The time-voltage plots show that K metal deposition is completed in 3.6 h for SA.Fe and 2.3 h for Al foil. The longer deposition time for SA.Fe suggests that the polarization electric field effectively guides K^+. The uniform, dense K metal coating on SA.Fe delays the deposition completion. Both materials exhibit Bragg peaks at 23.6° and 33.8°, corresponding to the (110) and (200) planes of K metal. However, SA.Fe shows a 1.5 h delay in the appearance of K metal signals, reflecting early dendrite suppression. During the stripping process, the Bragg peak for K metal on SA.Fe disappears within 1 h of charging, indicating a rapid and complete stripping mechanism. The charge transfer coefficient from Tafel analysis and the t_{K+} number support these observations. In contrast, the K metal signal on aluminum foil significantly attenuates during charging but persists weakly after 2 h, suggesting a hindered stripping process and residual K metal on the Al surface. The polarization electric field facilitates uniform K metal deposition and enhances stripping efficiency, resulting in superior dendrite suppression and electrochemical cycling performance for SA.Fe.

2.9. Applications of SA.Fe in PIB and PMB Full Cell System

To explore practical applications in PIBs and PMBs, SA.Fe and K metal coated SA.Fe (SA.Fe@K) are used as anodes with PTCDA as the cathode, creating two distinct full battery systems: SA.Fe//PTCDA and SA.Fe@K// PTCDA (**Figure 10a**). For PIB applications (Figure 10b–e), SA.Fe maintained a stable charging/discharging process at 1 A g^{-1} (Figure 10b), achieving a capacity of 124 mA h g^{-1}. After 200 cycles, it retained 118 mA h g^{-1}, corresponding to a 95.2% capacity retention. Robust K^+ adsorption and effective electron regulation mechanisms contribute to SA.Fe's performance. Additionally, SA.Fe//PTCDA exhibits an great rate performance (Figure 10c). SA.Fe maintains a capacity of 292 mAh g^{-1} at 0.3 A g^{-1}, demonstrating a 96.6% capacity retention after increases in current density. Galvanostatic profiles at different current densities (Figure 10d) show stable and reversible reactions. As the anode of PIBs, SA.Fe outperforms the reported carbon-based material, showing a better electrochemical performance (Figure 10e).

Figure 10f–i show that SA.Fe@K significantly improves stability in PMBs. At 200 mA g^{-1} (Figure 10f), SA.Fe@K//PTCDA achieves a capacity of 124 mAh g^{-1} and maintains ≈100% Coulombic efficiency. In contrast, pure K metal electrodes show a higher decay rate due to unstable SEI accumulation and dendrite formation. In rate performance (Figure 10g), SA.Fe@K exhibits a 6% increase in capacity after 75 cycles, demonstrating exceptional stability. Galvanostatic profiles at various current densities (Figure 10h) further confirm SA.Fe@K's outstanding performance. The uniform, dense K metal coating, guided by the polarization electric field, ensures a stable K^+ supply, maintaining consistent capacity throughout the cycling process. The Fe-N_4 coupling and polarization electric field significantly enhance K^+ storage and promote uniform, stable K metal deposition, which gives a rise to a better cycling stability and K^+ storage capability (Figure 10i).

3. Conclusion

In summary, SA.Fe significantly enhances K^+ kinetics in potassium-based batteries through the high metal loading and extensive Fe-N_4 coupling. The efficient horizontal electron transfer network supported by the conductive KB substrate boosts electron transfer efficiency, which accelerates electrochemical reactions at the electrode interface. The strong Fe-N-C coordination spontaneously generates a polar electric field, which enhances K^+ affinity, adsorption, and diffusion. The polar field effectively reduces K^+ migration resistance, improving charge transport. Moreover, the holistic regulation of K^+ kinetics led to a significant guiding effect for K^+, which optimizes the deposition behavior and suppresses the dendritic growth. These advancements optimize reaction pathways, lower the energy barrier for K^+ diffusion, and promote uniform K metal deposition, resulting in enhanced electrochemical performance and high energy storage capacity in PIBs and PMBs. The durable KB substrate further enhances cycle stability, while the holistic regulation of K^+ migration enables SA.Fe to achieve exceptional electrochemical performance. The coherent dipole–dipole Fe-N_4 polar coupling effectively overcomes hindered K^+ kinetics, marking a significant

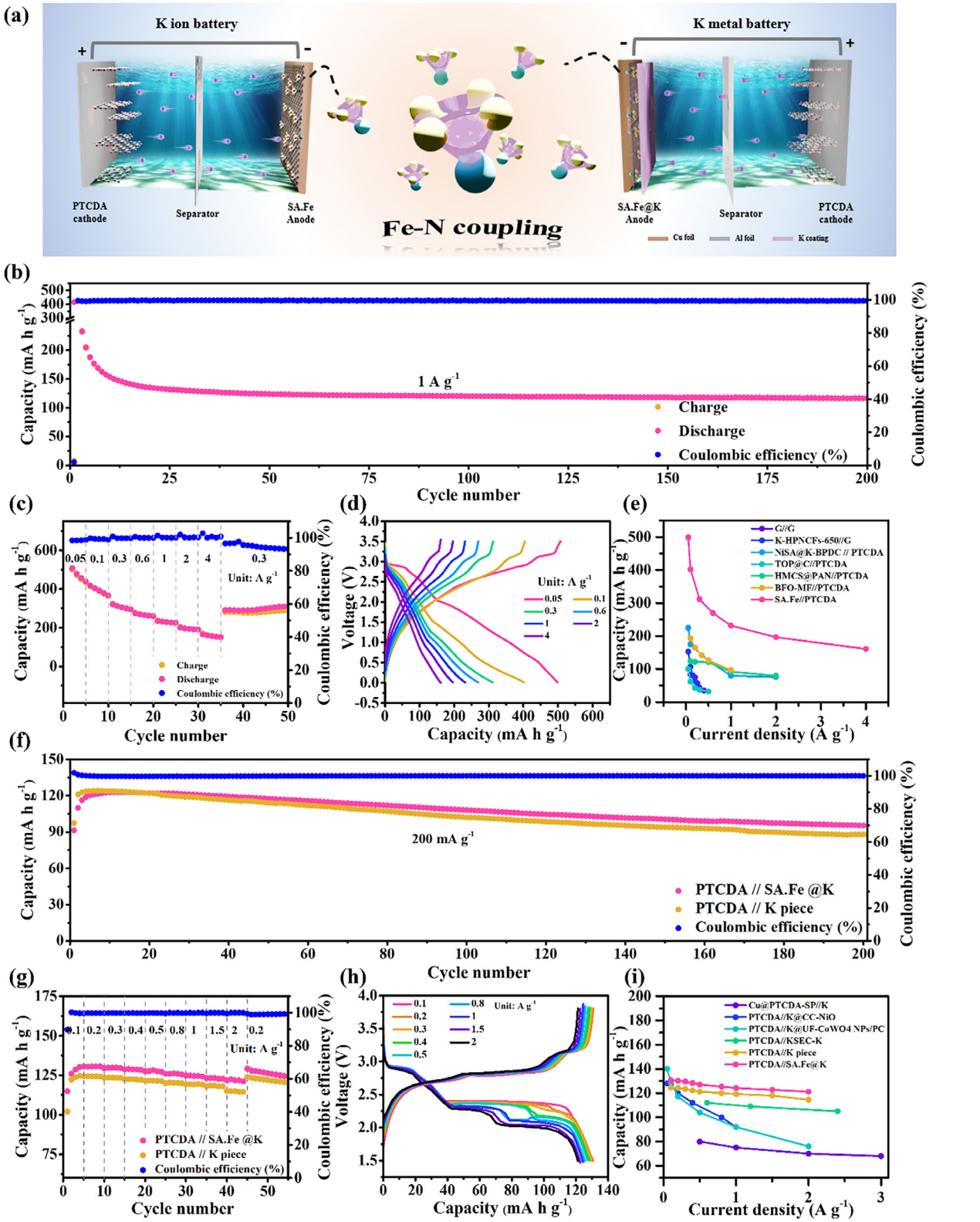

Figure 10. Applications of SA.Fe in PIB and PMB full cell system. a) The schematic illustration of dual applications of SA.Fe in both PIBs and PMBs. b) Cycling performance of the SA.Fe//PTCDA full cell at 1.0 A g^{-1}. c) Rate performance at various current densities and the corresponding d) Charge/discharge curves of the SA.Fe//PTCDA full cell. e) Comparison of the rate performance. f) Cycling performance of the SA.Fe@K//PTCDA full cell at 0.2 A g^{-1}. g) Rate performance at various current densities and the corresponding h) Charge/discharge curves of the SA.Fe@K//PTCDA full cell. i) Comparison of the rate performance.

advancement in electrochemical performance for both PIBs and PMBs.

Supporting Information

Supporting Information is available from the Wiley Online Library or from the author.

Acknowledgements

This work was supported by financial support from the 2030 Cross-Generation Young Scholars Program by the National Science and Technology Council (NSTC), through the grant of NSTC 113-2628-E-007-006.

Conflict of Interest

The authors declare no conflict of interest.

Author Contributions

Y.-Y.T. performed conceptualization, methodology, and data curation, and wrote the final manuscript. H.-Y.T. performed conceptualization, acquired resources, supervised the project, and wrote, reviewed, and edited the final manuscript.

Data Availability Statement

The data that support the findings of this study are available from the corresponding author upon reasonable request.

Keywords

anode, electric field regulation, metal deposition, potassium-based batteries, single atom

Received: November 29, 2024
Revised: February 4, 2025
Published online:

[1] X. Liu, J. Zhu, X. Wang, L. Yue, W. Wang, B. Wang, D. Shen, Y. Li, *Adv. Funct. Mater.* **2023**, *33*, 2209388.
[2] Y. Liu, Q. Wan, J. Gong, Z. Liu, G. Tao, J. Zhao, L. Chen, W. Li, X. Wei, L. Ni, *Small* **2023**, *19*, 2206400.
[3] M. Ma, S. Chong, K. Yao, H. K. Liu, S. X. Dou, W. Huang, *Matter* **2023**, *10*, 3220.
[4] Y. Xiao, F. Liu, H. Shi, L. Hou, G. Qin, C. Yuan, X. W. Lou, *Adv. Mater.* **2023**, *35*, 2301772.
[5] L. Yang, L. Guo, D. Yan, Y. Wang, T. Shen, D.-S. Li, M. E. Pam, Y. Shi, H. Y. Yang, *ACS Nano* **2023**, *17*, 6754.
[6] Z. Zhao, T. Xu, X. Yu, *Adv. Mater.* **2023**, *35*, 2208096.
[7] P.-W. Chien, C.-B. Chang, H.-Y. Tuan, *Energy Storage Mater.* **2023**, *61*, 102853.
[8] S.-F. Ho, H.-Y. Tuan, *Chem. Eng. J.* **2023**, *452*, 139199.
[9] Y.-Y. Hsieh, K.-T. Chen, H.-Y. Tuan, *Chem. Eng. J.* **2021**, *420*, 130451.
[10] Y. Y. Hsieh, H. Y. Tuan, *Small* **2023**, *19*, 2305342.
[11] C.-Y. Tsai, C.-H. Chang, T.-L. Kao, K.-T. Chen, H.-Y. Tuan, *Chem. Eng. J.* **2021**, *417*, 128552.
[12] H.-Y. Tuan, A. Ghezelbash, B. A. Korgel, *Chem. Mater.* **2008**, *20*, 2306.
[13] F.-W. Yuan, H.-J. Yang, H.-Y. Tuan, *J. Mater. Chem.* **2011**, *21*, 13793.
[14] Y. An, Y. Tian, H. Shen, Q. Man, S. Xiong, J. Feng, *Energy Environ. Sci.* **2023**, *16*, 4191.
[15] A. Li, Y. Man, J. Liao, L. Duan, X. Ji, X. Zhou, *Nano Lett.* **2023**, *23*, 10066.
[16] Y. Feng, A. M. Rao, J. Zhou, B. Lu, *Adv. Mater.* **2023**, *35*, 2300886.
[17] J. Park, Y. Jeong, H. Kang, T. Y. Yu, X. Xu, Y. Liu, S. Xiong, S. H. Lee, Y. K. Sun, J. Y. Hwang, *Adv. Funct. Mater.* **2023**, *33*, 2304069.
[18] Q. Shen, Y. He, J. Wang, *J. Mater. Chem. A* **2023**, *11*, 9829.
[19] M. Tang, S. Dong, J. Wang, L. Cheng, Q. Zhu, Y. Li, X. Yang, L. Guo, H. Wang, *Nat. Commun.* **2023**, *14*, 6006.
[20] X. Wen, W. Feng, X. Li, J. Yang, R. Du, P. Wang, H. Li, L. Song, Y. Wang, M. Cheng, *Adv. Mater.* **2023**, *35*, 2211690.
[21] D. Zhang, X. Ma, L. Wu, J. Wen, F. Li, J. Zhou, A. M. Rao, B. Lu, *Adv. Energy Mater.* **2023**, *13*, 2203277.
[22] J. Chen, S. Lei, S. Zhang, C. Zhu, Q. Liu, C. Wang, Z. Zhang, S. Wang, Y. Shi, L. Yin, *Adv. Funct. Mater.* **2023**, *33*, 2215027.
[23] Y. Jiang, S. Lu, J. Jiang, M. Li, Y. Liao, Y. Xu, S. Huang, B. Zhao, J. Zhang, *Small* **2023**, *19*, 2300411.
[24] S. Zhang, X. Zhuang, X. Du, X. Zhang, J. Li, G. Xu, Z. Ren, Z. Cui, L. Huang, S. Wang, *Adv. Mater.* **2023**, *35*, 2301312.
[25] P. Cai, K. Wang, X. He, Q. Li, Z. Zhang, M. Li, H. Li, M. Zhou, W. Wang, K. Jiang, *Energy Storage Mater.* **2023**, *60*, 102835.
[26] J. Liu, L. Zhang, K. Wang, C. Jiang, C. Zhang, N. Wang, *Small* **2024**, *20*, 2400093.
[27] H. Shan, J. Qin, Y. Ding, H. M. K. Sari, X. Song, W. Liu, Y. Hao, J. Wang, C. Xie, J. Zhang, *Adv. Mater.* **2021**, *33*, 2102471.
[28] C. Zhang, F. Han, F. Wang, Q. Liu, D. Zhou, F. Zhang, S. Xu, C. Fan, X. Li, J. Liu, *Energy Storage Mater.* **2020**, *24*, 208.
[29] H. Ding, J. Wang, J. Zhou, C. Wang, B. Lu, *Nat. Commun.* **2023**, *14*, 2305.
[30] Y. Liu, Y. Shi, C. Gao, Z. Shi, H. Ding, Y. Feng, Y. He, J. Sha, J. Zhou, B. Lu, *Angew. Chem.* **2023**, *135*, 202300016.
[31] L. Tu, Z. Zhang, Z. Zhao, X. Xiang, B. Deng, D. Liu, D. Qu, H. Tang, J. Li, J. Liu, *Angew. Chem., Int. Ed.* **2023**, *62*, 202306325.
[32] S. Xie, W. Xie, Q. Zhang, X. Cheng, X. Ouyang, B. Lu, *Adv. Funct. Mater.* **2023**, *33*, 2302880.
[33] L. Song, S. Zhang, L. Duan, R. Li, Y. Xu, J. Liao, L. Sun, X. Zhou, Z. Guo, *Angew. Chem., Int. Ed.* **2024**, *63*, 202405648.
[34] Y. Li, H. Jia, U. Ali, H. Wang, B. Liu, L. Li, L. Zhang, C. Wang, *Adv. Energy Mater.* **2023**, *13*, 2301643.
[35] Y. Chen, N. Fu, B. Shen, Y. Yan, W. Shao, T. Wang, H. Xie, Z. Yang, *Small* **2023**, *19*, 2207423.
[36] X. Guo, H. Gao, S. Wang, G. Yang, X. Zhang, J. Zhang, H. Liu, G. Wang, *Nano Lett.* **2022**, *22*, 1225.
[37] Y. Li, A. Zhu, G. Peng, J. He, D. Jia, J. Qiu, X. He, *Adv. Funct. Mater.* **2024**, *34*, 2410212.
[38] B. Xiao, Z. Sun, H. Zhang, Y. Wu, J. Li, J. Cui, J. Han, M. Li, H. Zheng, J. Chen, *Energy Environ. Sci.* **2023**, *16*, 2153.
[39] W. Xu, H. Li, X. Zhang, T. Y. Chen, H. Yang, H. Min, X. Shen, H. Y. Chen, J. Wang, *Adv. Funct. Mater.* **2024**, *34*, 2309509.
[40] G.-Z. Yang, Y.-F. Chen, B.-Q. Feng, C.-X. Ye, X.-B. Ye, H. Jin, E. Zhou, X. Zeng, Z.-L. Zheng, X.-L. Chen, *Energy Environ. Sci.* **2023**, *16*, 1540.
[41] J. Zhu, J. Li, R. Lu, R. Yu, S. Zhao, C. Li, L. Lv, L. Xia, X. Chen, W. Cai, *Nat. Commun.* **2023**, *14*, 4670.
[42] T. Anusuya, V. Kumar, *Phys. Chem. Chem. Phys.* **2023**, *25*, 262.
[43] S.-S. Wang, Z.-M. Liu, X.-W. Gao, X.-C. Wang, H. Chen, W.-B. Luo, *ACS Appl. Mater. Interfaces* **2023**, *15*, 57165.
[44] X. Wang, Z. Xiao, K. Han, X. Zhang, Z. Liu, C. Yang, J. Meng, M. Li, M. Huang, X. Wei, *Adv. Energy Mater.* **2023**, *13*, 2202861.
[45] J. Zhang, Z. Du, T. Yan, F. Zeng, Z. Xu, J. Xu, Z. Meng, X. Hu, J. Zhao, H. Tian, *Energy Storage Mater.* **2023**, *60*, 102831.

[46] F. Liu, J. Meng, G. Jiang, J. Li, H. Wang, Z. Xiao, R. Yu, L. Mai, J. Wu, *Matter* **2021**, *4*, 4006.
[47] Y. Wang, S. Zuo, C. Zeng, J. Wan, Z. Yan, J. Yi, *Chemosphere* **2023**, *344*, 140331.
[48] Z. Gao, S. Tao, L. Zhu, T.-Y. Chen, H. Min, X. Shen, H. Yang, H.-Y. Chen, J. Wang, *J. Colloid Interface Sci.* **2023**, *649*, 203.
[49] F. Luo, J. Zhu, S. Ma, M. Li, R. Xu, Q. Zhang, Z. Yang, K. Qu, W. Cai, Z. Chen, *Energy Storage Mater.* **2021**, *35*, 723.
[50] X. Xie, L. Peng, H. Yang, G. I. Waterhouse, L. Shang, T. Zhang, *Adv. Mater.* **2021**, *33*, 2101038.
[51] M. Chen, Y. Cao, C. Ma, H. Yang, *Nano Energy* **2021**, *81*, 105640.
[52] Y. Chen, B. Xi, M. Huang, L. Shi, S. Huang, N. Guo, D. Li, Z. Ju, S. Xiong, *Adv. Mater.* **2022**, *34*, 2108621.
[53] H. Deng, L. Wang, S. Li, M. Zhang, T. Wang, J. Zhou, M. Chen, S. Chen, J. Cao, Q. Zhang, *Adv. Funct. Mater.* **2021**, *31*, 2107246.
[54] L. Li, Y. Li, Y. Ye, R. Guo, A. Wang, G. Zou, H. Hou, X. Ji, *ACS Nano* **2021**, *15*, 6872.
[55] X. Ma, N. Xiao, J. Xiao, X. Song, H. Guo, Y. Wang, S. Zhao, Y. Zhong, J. Qiu, *Carbon* **2021**, *179*, 33.
[56] K. M. Diederichsen, E. J. McShane, B. D. McCloskey, *ACS Energy Lett.* **2017**, *2*, 2563.
[57] H. Yang, W. Wang, Z. Huang, Z. Wang, L. Hu, M. Wang, S. Yang, S. Jiao, *Adv. Mater.* **2024**, *36*, 2401008.
[58] Q. Yao, C. Zhu, *Adv. Funct. Mater.* **2020**, *30*, 2005209.
[59] S. Zhao, Z. Liu, G. Xie, Z. Guo, S. Wang, J. Zhou, X. Xie, B. Sun, S. Guo, G. Wang, *Energy Environ. Sci.* **2022**, *15*, 3015.
[60] Y. Bai, Z. Wu, Q. Lv, W. Sun, W. Liang, X. Xia, H. Zhang, C. M. Li, *J. Colloid Interface Sci.* **2025**, *679*, 1311.
[61] L. Xu, C. Huang, Z. Hua, L. Chen, *Energy Storage Mater.* **2023**, *61*, 102888.
[62] H. Yu, G. Zhang, D. Zhang, R. Yang, X. Li, X. Zhang, G. Lian, H. Hou, Z. Guo, C. Hou, *Adv. Energy Mater.* **2024**, *14*, 2401509.
[63] Z. Wang, J.-F. Wu, W. Zhou, Y. Mo, S. Chen, T. Zhou, W. Shen, B. Ren, P. Huang, J. Liu, *ACS Energy Lett.* **2024**, *9*, 4534.
[64] J. F. Wu, W. Zhou, Z. Wang, W. W. Wang, X. Lan, H. Yan, T. Shi, R. Hu, X. Cui, C. Xu, *Adv. Mater.* **2023**, *35*, 2209833.
[65] Z. Yu, K. Fan, Q. Liu, D. Wang, C. Chen, Y. Zhu, H. Huang, B. Zhang, *Adv. Funct. Mater.* **2024**, *34*, 2315446.
[66] D.-T. Zhang, M.-C. Liu, M.-P. Li, Z.-Z. Yuan, Y.-X. Hu, H. Chen, C.-Y. Li, L.-B. Kong, K. Zhao, J.-Q. Ren, *Chem. Eng. J.* **2024**, *482*, 148896.
[67] D.-T. Zhang, W.-J. Shi, M.-P. Li, H. Chen, C.-Y. Li, Y.-X. Hu, L.-B. Kong, K. Zhao, J.-Q. Ren, H.-T. Xue, *J. Energy Storage* **2024**, *77*, 109903.
[68] J. L. Zhou, L. K. Zhao, Y. Lu, X. W. Gao, Y. Chen, Z. M. Liu, Q. F. Gu, W. B. Luo, *Adv. Funct. Mater.* **2024**, *34*, 2403754.
[69] E. Zhang, X. Hu, L. Meng, M. Qiu, J. Chen, Y. Liu, G. Liu, Z. Zhuang, X. Zheng, L. Zheng, *J. Am. Chem. Soc.* **2022**, *144*, 18995.